PCCP

Probing the Effects of Ester Functional Group, Alkyl Side Chain Length and Anion on Bulk Nanostructure of Ionic Liquids: A Computational Study

Probing the Effects of Ester Functional Group, Alkyl Side Chain Length and Anion on Bulk Nanostructure of Ionic Liquids: A Computational Study

Mostafa Fakhraee
Department of Chemistry, Sharif University of Technology,
Tehran, 11365-11155, Iran

Mohammad Reza Gholami*
Department of Chemistry, Sharif University of Technology,
Tehran, 11365-11155, Iran

(*Corresponding author e-mail: gholami@sharif.edu)

Abstract

The effects of ester addition on nano structural properties of biodegradable ILs composed of 1-alkoxycarbonyl-3-alkyl-imidazolium cation ($[C_1COOC_nC_1im]^+$, n=1, 2, 4) combined with $[Br]^-$, $[NO_3]^-$, $[BF_4]^-$, $[PF_6]^-$, $[TfO]^-$, and $[Tf_2N]^-$ were explored by using the molecular dynamics (MD) simulations and quantum theory of atoms in molecules (QTAIM) at 400 K. Various thermodynamic properties of these ILs were extensively computed in our earlier work (*Ind. Eng. Chem. Res.*, 2015, **54**, 11678–11700). Nano-scale segregation analysis demonstrates the small spherical hydrocarbon island-like formation within the continuous ionic domain for ILs with short alkyl side chain ($[C_1COOC_1C_1im]$), and sponge-like nanostructure for the compound with long alkyl side chain ($[C_1COOC_4C_1im]$). Ester-functionalized ILs with ethyl side chain ($[C_1COOC_2C_1im]$) are the turning point between two different morphologies. Non-polar channels were observed for $[C_1COOC_4C_1im]$ ILs composed of smaller anions such as [Br] and $[NO_3]$, whereas clustering organization was found for the other anions. Constitution of the spherical micelle-like nanostructure was seen for lengthened cations. Finally, the incorporation of an ester group into the alkyl side chain of cation leads to stronger segregation between charged and uncharged networks, which consequently increased the possibility of self-assembly and micelle formation.

Keywords: biodegradable ionic liquid, molecular dynamics simulation, quantum theory of atoms in molecules, spherical micelle-like nanostructure.

1. INTRODUCTION

Environmental problems of volatile organic solvents have led to great interest for exploring an appropriate alternatives.[1-4] Ionic liquids (ILs) have been considered suitable candidates for replacement of these organic compounds,[5-7] owing to their negligible vapour pressure, non-flammability, and excellent thermal and chemical stability.[8,9] Moreover, high ionic conductivity and wide electrochemical window of ILs are the driving force for their applications in catalysis, synthesis of metal nanoparticles, separation, extraction techniques, and electrochemistry.[8-12]

An IL is composed of organic cation and organic/inorganic anion, therefore, its physicochemical properties can be adjusted in order to use in specific applications.[13-15] The most recent studies focused on imidazolium-based ILs due to having tuneable properties.[1-15] Recently, functionalized imidazolium-based ILs have been synthesized and investigated by both computational and experimental methods owing to their high potential to absorb some of the greenhouse gases such as CO_2, SO_2, O_2, and N_2.[2,3,13,16,17] Among this class of ILs, ester-functionalized imidazolium-based ILs due to their high biodegradation potential, have been recently synthesized and investigated experimentally.[18-23] Thermodynamic properties of ester functionalized ILs were extensively investigated in our earlier work.[24] To authors' knowledge a few investigations have been focused on the nano-structural properties of these biodegradable ILs.[21,25] It has been proved that the structural properties of ILs can be evaluated by using MD simulations from microscopic point of view.[2,3,5-9,11,13,14,25] In this context, the main aim of the present study is to elucidate the effects of ester functional group, cation side chain length and anion substitution on the bulk nano-structural properties of ester functionalized ILs by using MD simulations and quantum theory of atoms in molecules (QTAIM) analysis. These ILs are as follows: 3-methyl-1-(methoxycarbonylmethyl)imidazolium ($[C_1COOC_1C_1im]^+$), 3-methyl-1-(ethoxycarbonylmethyl) imidazolium ($[C_1COOC_2C_1im]^+$), and 3-methyl-1-(buthoxycarbonylmethyl) imidazolium

([$C_1COOC_4C_1im$]$^+$) cations paired with [Br]$^-$, [NO_3]$^-$, [BF_4]$^-$, [PF_6]$^-$, [TfO]$^-$, and [Tf_2N]$^-$ anions (Fig. 1). In addition, nano-scale structuring and micelle formation of selected ILs in their bulk phase were extensively studied.

2. COMPUTAIONAL METHODS

2.1 Ab initio calculations and QTAIM analysis

It should be noted that H_n sites of imidazolium-based cations become more acidic in the presence of ester group. Therefore the acidic strength of these sites can be simultaneously compared by optimizing [$C_1COOC_nC_1im$][anion]$_3$ clusters. Also, more realistic cation-anion organization pattern are provided from aforementioned clusters. Hence these structures were optimized at B3LYP/6-311++G(d,p) level of theory using Gaussian package of program[26]. Subsequently, the magnitude order of H_n-anion interactions of these clusters was quantitatively estimated from QTAIM analysis[27] by means of the MultiWFN 3.1 program.[28]

2.2. Molecular dynamics simulations

A detailed explanation of the utilized force field parameters and performed simulations was provided in the Electronic Supplementary Information. Initial atomic configurations of classical molecular dynamic simulations in this study were taken from our previous study.[24] Target systems were equilibrated 0.3 ns followed by a production run of 1.2 ns. The considered temperature (400 K) is rationalized to improve evaluation of structural properties of these sluggish compounds.

3. RESULTS AND DISCUSSION

3.1 Quantum theory of atoms in molecules

The optimized clusters were confirmed to be minima by frequency calculations. Fig. 2 demonstrates the optimized geometries of [$C_1COOC_nC_1im$][anion]$_3$ along with their cage critical points (CCPs), ring critical points (RCPs) as well as bond critical points (BCPs). Additionally,

topological properties at BCPs, including the electron density (ρ_b) and its Laplacian ($\nabla^2\rho_b$), kinetic-energy density (G_b), potential-energy density (V_b), total energy density ($H_b=G_b+V_b$), the ratio of the kinetic-energy density, and the potential-energy density ($-G_b/V_b$), were computed and collected in Tables 1 and 2. It should be emphasized that the index of each BCP in Tables 1 and 2 corresponds to the determined labels in Fig. 2. Due to the fact that the elongation of alkyl side chain does not have a significant effect on aforesaid topological properties of these ILs, QTAIM analysis was merely performed on [$C_1COOC_1C_1im$][anion]$_3$ clusters. Topological analyses for the other ILs are available in Table S6, Fig. S1, and Fig. S2 of the Electronic Supplementary Information. In fact, ρ_b is a criterion of the bond strength.[29,30] Larger ρ_b values are associated with the greater interaction energies. To be more precise, ρ_b is greater than 0.20 au in shared (covalent) bonding and less than 0.10 au in a closed-shell interaction.[29,30] According to Tables 1 and 2, the magnitude order of ρ_b values are in the range of 10^{-2}-10^{-3} au, which is related to the closed-shell interactions of H_n-anion. The stronger H_n-anion interaction is attributed to the H_2-anion, followed by H_4, H_5, and H_6 sites and the weaker H_n-anion is attributed to H atoms of alkyl side chain.

The Laplacian of electron density ($\nabla^2\rho_b$) exhibits the curvature of the electron density in three-dimensional space at the BCP of the atomic interaction.[29,30] In general, a negative $\nabla^2\rho_b$ shows a local concentration of the electron density likes the covalent interaction, whereas closed-shell bonding corresponds to a positive value of $\nabla^2\rho_b$.[30,31] The achieved $\nabla^2\rho_b$ values of H_n-anion interactions are positive and have the strong H bonding character.[32]

The ratio of G_b and V_b at the critical point ($-G_b/V_b$) can be utilized as a criterion for determining covalent or non-covalent interactions.[30,31] When this ratio is less than 0.5, interaction is known as a shared covalent and when its value is in the range between 0.5 to 1, interaction is recognized as

partly covalent. Finally, when this ratio is greater than 1, it characterizes a closed-shell interaction.[30] From the gained findings of Tables 1 and 2, $-G_b/V_b$ values are greater than 1, suggesting that the closed shell interaction plays an important role in the H_n-anion interactions.

The total energy density is another suitable index which is used to understand the weak non-bonded interactions.[30] It is already known that for positive H_b value, the accumulation of electrons at the BCP is destabilized, and therefore, electrostatic interactions are dominant.[30] Whereas the accumulation of electrons at the BCP is stabilized when H_b has a negative value, which is a characteristic of shared interactions.[30] As shown in Tables 1 and 2, all H_b values are positive, proposing that the H_n-anion interactions have a prevailing electrostatic character.

In addition, electron location function (ELF) [33-36] and localized orbital locator (LOL) [30,31] were computed through BCPs. As it can be seen in Tables 1 and 2, ELF and LOL values are nearly located within the 10^{-2} to 10^{-1} range, confirming closed-shell interactions for H_n-anion. ELF and LOL results were also plotted in Figs. S3 and S4 of the Electronic Supplementary Information for $[C_1COOC_1C_1im][Br]$, $[C_1COOC_1C_1im][NO_3]$, and $[C_1COOC_1C_1im][BF_4]$ through their BCPs.

In summary, QTAIM analysis indicated that the stronger H_n-anion interactions is occurred via H_2, followed by H_4, H_5, and H_6 sites, respectively and weaker interactions are constituted when anions move toward H atoms of alkyl side chain of cations. Moreover, H_6-anion interionic interactions are more desirable than H_{10}-anion owing to the presence of ester functional group. Consequently, the direct H_2-anion interaction becomes weaker, while H_6-anion is found to be stronger than corresponding interactions in traditional imidazolium-based ILs.[37-40]

3.2. Molecular dynamics simulations

3.2.1. Average structure of cations

The average structures of cations along with their intra-molecular H bonds between O_8-H_n sites are shown in Fig. 3. As it can be observed, the intra-molecular hydrogen bonds are simultaneously constituted between O_8-H_2, O_8-H_5, and O_8-H_{11} sites. The O_8 site of ester-functionalized is placed between H_2 and H_5 acidic sites of imidazolium-ring at approximately equal distances (within range of 3-4 Å). To be more precise, O_8 is mostly biased towards the H_2 site in $[C_1COOC_1C_1im][PF_6]$, $[C_1COOC_2C_1im][PF_6]$, $[C_1COOC_1C_1im][TfO]$, $[C_1COOC_4C_1im][TfO]$ as well as for ILs containing $[Tf_2N]$ anions, while it mainly attracted into the H_5 atomic site in $[C_1COOC_4C_1im][NO_3]$, $[C_1COOC_2C_1im][BF_4]$ ILs. Furthermore, the strong correlation between O_8-H_{11} sites can be observed nearly within range of 2.3-3 Å for all selected ILs, which is in excellent agreement with those obtained by *ab initio* calculations in our previous study.[24] In addition, another intra-molecular H bonding is cohesively formed between O_8 and H_{12} sites in $[C_1COOC_2C_1im][NO_3]$, $[C_1COOC_2C_1im][Tf_2N]$, $[C_1COOC_4C_1im][Br]$, and $[C_1COOC_4C_1im][BF_4]$ ILs. Moreover, the lowest association between O_8 and H_n sites is formed via H_6 site owing to their opposite orientation. The weaker intra-molecular interaction between O_8 and H_{10}, H_{13}, and H_{14} sites are also shown in Fig. 3.

Another set of intra-molecular H bonds are constitute via O_9-H_n sites (Fig. 4). A direct O_9-H_{12} intra-molecular H bonding is approximately positioned within range of 2-3 Å for an average structure of $[C_1COOC_4C_1im]$. It should be stressed that in $[C_1COOC_4C_1im][PF_6]$ the O_9-H_{12} interaction is replaced by O_9-H_{13}. In addition, the other intra-molecular interactions of O_9-H_2, O_9-H_4, O_9-H_5, O_9-H_{10}, O_9-H_{13}, O_9-H_{14} sites occur at distances around 4-5, 6-7, 4-5, 7-8, 3.9-4.2, and 4.5-5.2 Å, respectively.

3.2.2. Nano-scale segregation

Nano-scale organization in imidazolium-based ILs corresponding to a segregation of the polar and non-polar domains have been already reported, using various theoretical and experimental methods.[41-62] The segregation of ILs into the charged and uncharged domains provides their solavtion characteristics, due to impressive effects of such dual structure and also through the types of interactions with both ionic and non-polar solutes.[41-62] The color code offered by Canongia Lopes and Pádua[41,42] was implemented to distinguish the high charge density (in red color) and low charge density (in green color) regions. According to the gained results from electrostatic potential map (ESP)[25] (Figs. S5 and S6 of the Electronic Supplementary Information), all atoms of an anion plus atoms of the imidazolium ring accompanied with their connected atoms as well as the atoms of ester functional group form the regions considered to be of high charge density, while the neutral alkyl chain of cation (C_{11} to C_{14}) constitute the regions considered to be of low charge density. Figs. 5 and 6 demonstrate the morphology of charged and non-polar domains of selected ILs. Unexpectedly, for ILs with short alkyl side chain ([$C_1COOC_1C_1im$]), small spherical hydrocarbon island-like is constituted within the continuous ionic domain, whilst, sponge-like nanostructure for the compound with long alkyl side chain ([$C_1COOC_4C_1im$]) can be observed, in that, longer alkyl side chain more tends to be excluded from the polar network. Segregation of polar and apolar domains is more pronounced with lengthening alkyl chain, indicating that ion amphiphilicity is the main factor in structuring order of ester-functionalized IL. Specifically, non-polar channels are observed for [$C_1COOC_4C_1im$] ILs composed of smaller anions such as [Br] and [NO_3], whereas clustering organization can be found for the other ILs. In fact, small anions with a strong localized charge increase the aggregation of cation side chains. This result is in good agreement with the reported finding by Kirchner *et al.* [63], where side chain fluorination and anion effect on the structure of 1-butyl-3-

methylimidazolium ILs were comprehensively studied. Finally, ester-functionalized ILs with

ethyl side chain ($[C_1COOC_2C_1im]$) are the turning point between two different morphologies.

More precise identification of segregation of polar and non-polar regions was inspected by

analyzing radial distribution functions (RDFs) of the terminal carbon atoms (C_n-C_n) in Fig. 7.

More details are shown in Fig. S19 of the Electronic Supplementary Information. In addition, the

aggregation size ($N^{\dagger}$) of cation clusters was computed according to Eq. 2 [63]

$$\left\langle N^{\dagger} \right\rangle = 1 + 4\pi \int_0^{r_{\min}} \rho_C \, g_{C-C}(r) \, r^2 \, dr \qquad (2)$$

where $g_{c\text{-}c}(r)$ is the C_n-C_n RDF, r_{min} implies to the first minimum of corresponding RDF, and ρ_c

denotes the atom density of terminal carbon atom. Table 3 represents the numerical values of

aggregation size ($N^{\dagger}$) of C_n-C_n RDFs. It can be seen that $N^{\dagger}$ gradually increased with lengthening

alkyl side chain, especially for ester-functionalized ILs composed of smaller anions such as [Br]

and [NO_3]. These findings are comparable with the reported aggregation size and C_n-C_n RDFs by

Kirchner *et al.* [63]. Interestingly, C_{11}-C_{11} RDFs for $[C_1COOC_1C_1im]$ show higher intensity at

maximum point than matching RDFs for $[C_1COOC_2C_1im]$ and $[C_1COOC_4C_1im]$ (Fig. S19). A

similar trend is found for C_{12}-C_{12}. The most outstanding feature of aforementioned RDFs is the

strong correlation between the terminal C atoms of the alkyl side chain, which becomes stronger

for lengthened cation. Furthermore, C_n-C_n RDFs of $[C_1COOC_4C_1im]$ demonstrate higher

possibility in the following order: C_{11}-$C_{11} < C_{12}$-$C_{12} < C_{13}$-$C_{13} < C_{14}$-C_{14}. From the results we can

conclude that head and ester groups accompanied by their anions are homogeneously distributed

owing to their similar net charges. Whereas neutral tail groups tend to stay closer, with the

equilibrium average distances are decided only by their short-range interactions. Briefly, the

distribution of cations with short alkyl side chain in the bulk phase is mostly determined by the

charged head groups, where the tail groups do not have enough collective attractive energy to

aggregate. The interactions between tail groups become greater with lengthening alkyl side linkage due to the satisfaction of both requirements for segregation of the head and tail groups.

3.2.3 Micelle-like nanostructure

A snapshot of selected sections of the equilibrated simulation box of $[C_1COOC_nC_1im][Br]$ are qualitatively indicated in Fig. 8. The spherical micelle-like nanostructure can be easily found for ILs with the longest alkyl side chain length, because head groups and associated anions are stacked together homogeneously, and tail groups are oriented toward the center of sphere. In addition, $[C_1COOC_2C_1im]$ cation with a critical asymmetry, forms slight bicontinuous phase morphology from self-assembly of polar and apolar groups in the bulk, while chaotic packing is seen for ILs composed of the nonamphiphilic cation ($[C_1COOC_1C_1im]$). It may be caused by the reduction of tendency to create a self-assemble of charged and uncharged moieties, which is mostly governed by alkyl side chain length. Fig. 9 indicates self-assembly of the largest cation from the different parts of equilibrated simulation box of $[C_1COOC_4C_1im][Br]$ with high resolution.

Several investigations already focused on the effects of alkyl side chain length of ions on tail aggregation in liquid phase of various set of ILs by means of the MD simulation and experimental method, especially including X-ray diffraction, small- and wide-angle X-ray scattering (SAXS and WAXS).[25,41-62] A brief review of nanostructure organization of different sets of ILs is available in the Electronic Supplementary Information. These investigations demonstrated that bicontinuous phase morphology due to the self-assembly of polar and apolar groups in the bulk can be clearly observed for C_4 alkyl side linkage, onward.[25,41-62] While an ester-functionalized IL containing more than or equal to C_2 shows explicit segregation of charge- and uncharged domains. This result is good consistency with experimental results reported by

Garcia *et al.*,[21] where thermal stability, aggregation behavior in aqueous medium, and antimicrobial activity of two series of long chain imidazolium- and pyridinium-based ILs (C_n= 6, 8, 10, 12, 14) consisting an ester functional group paired with [Br] were investigated. They showed that the incorporation of an ester functional group promotes adsorption at the air/water interface, micelle formation, and antimicrobial activity.[21]

3.2.4. Cation-anion interaction

The site-site cation-anion RDFs were utilized to characterize the bulk microstructure of explored ILs. The radial distribution function between particle type of *i* and *j* can be defined using Eq. 2, as follows:[64,65]

$$g_{ij}(r) = \frac{n_{ij}(r)}{4\pi r^2 \rho_j \, dr} = \frac{V}{N_i N_j} \sum_{i=1}^{N_i} \sum_{j=i+1}^{N_j} \left\langle \delta\left(r - \left|\vec{r}_i(t) - \vec{r}_j(t)\right|\right) \right\rangle_t \tag{2}$$

where ρ_j is the number density of particles *j*, and $n_{ij}(r)$ implies to the number of particles of type *j* between distance *r* and *r+dr* from a particle of type *i*. Actually, ρ_j can be directly estimated from the mole fraction of particle *j* (x_j) and the total number density of simulation box (ρ) as $\rho_j = x_j. \rho$.[63] On right side of Eq. 2, r_i-r_j is the distance between atoms of type *i* and *j*, and the bracket indicates an ensemble average.

Fig. 10 (a) represents the cation-anion site-site RDFs , such that the nearest atoms to the center of mass of the cations (C_2) and anions (N atom for [NO_3] and [Tf_2N], S atom for [TfO], B atom for [BF_4], and P atom for [PF_6]) were chosen. Fig. 10 (b) depicts the cation-anion center-of-mass RDFs for [$C_1COOC_4C_1im$][Br] ILs. The corresponding RDFs for the other selected ILs are depicted in Fig. S7 of the Electronic Supplementary Information. The intensity of C_2-anion peaks increased with elongation of alkyl side chain of cation, while the opposite trend is found for the cation-anion center-of-mass RDFs. The center-of-mass RDFs begin at smaller distances when alkyl side chain is lengthened, which is a sign of stronger cation-anion correlation in their bulk

phase. Several characteristic parameters of these RDFs, such as location of their first maximum

(max_1) and minimum (min_1) as well as their coordination numbers in the first shell (N) have been

summarized in Table 3. It should be noted that two consecutive peaks of C_2-anion RDFs were

considered in order to calculate their characteristic parameters. According to Table 3, elongation

of alkyl side chain of cation does not remarkably influence the estimated coordination number.

Fig. 10 (c) demonstrates the H_n-anion RDFs of $[C_1COOC_4C_1im][Br]$ ILs. According to the

similar trends of H_n-anion RDFs, corresponding results for the other ILs are shown in Figs. S8 to

S10 of the Electronic Supplementary Information. It should be emphasized that the strong site of

an anion with negative charge concentration was selected based on the yielded results of ESP

(Figs. S5 and S6 of the Electronic Supplementary Information). Herein, O atoms were chosen for

$[NO_3]^-$, $[TfO]^-$, and $[Tf_2N]^-$ and also F atoms were noticed as interactive sites of $[BF_4]^-$ and $[PF_6]^-$

anions. The achieved results of H_n-anion RDFs showed that the strongest association of cation-

anion is attributed to the ILs composed of the smaller anions such as $[Br]^-$ and $[NO_3]^-$. Cation-

anion RDFs indicate that bulk phase becomes more organized with increasing the alkyl side

chain length of cation. This observation can be explained by the homogenous distribution of the

charged anions and head groups of the cations due to their strong electrostatic interactions,

whereas the collective short range interactions are the driving force for aggregation of the neutral

tail groups. In summary, the formation of micelle-like nanostructure seems to be responsible for

this observation, which was previously verified by the nano-scale segregation (Figs. 5 and 6) and

micelle-like nanostructure analysis (Figs. 8 and 9). The acidic H sites of cation such as H_2, H_5,

H_4, H_6, and H_{10} can be considered to be the interactive sites of cations, respectively. The first

peak intensity of H_n-anion RDFs (2-3 Å) decreased in the following order: $H_2 > H_5 \geq H_4 \geq H_6 >$

H_{10} and a reverse trend is observed for the second peak. Almost a similar trend as for the first

peak is held for the third one. ILs composed of [Br] anion have a roughly different organization structure than the other ILs, which is supported by the sharpness and intensity of the H_n-Br RDFs in Fig. 10 (c). Furthermore, H_n-Br RDFs starts at ~2.5 Å, whereas for the other bulkier anions begin at shorter distance (~2 Å). This may be related to the higher atomic volume of Br atom than H, C, N, and O atoms. While, three or more consecutive and broad peaks can be found for H_n-anion RDFs, H_2-Br RDFs show two distinguished peaks in which the first one is located in the range of 2.5-3 Å and the second one is positioned at farther distances (~6 Å). This is an evidence of the strong cation-Br correlation at the first shell and consequently weaker interionic interactions at the second one. A similar template is approximately observed for the other H_n-anion RDFs, where the second and third peaks are almost located at 4.5 Å and 6 Å, respectively. Even though, H_6 and H_{10} sites have almost a homologous position, preferred H_6-anion interactions can be revealed from the H_n-anion RDFs. According to these RDFs, the weakest H_n-anion interactions are ascribed to the H atoms of neutral alkyl chain, roughly in the following order of intensity: $H_{11} > H_{12} > H_{13} > H_{14}$, which appeare as broad and small peaks. These findings is in excellent agreement with QTAIM analysis of $[C_1COOC_nC_1im][anion]_3$ conformers and the optimized geometries of the isolated ion pairs in our previous work.[24]

A more detailed analysis of the cation-anion arrangement was obtained by providing C_7-anion and C_n-anion (n=11, 12, 14) RDFs in Fig. S11 of the Electronic Supplementary Information. Additionally, site-site RDFs between C_n (n=11, 12, 13) sites of $[C_1COOC_4C_1im]$ ILs and nearest atoms to the center of masses of anions are shown in Fig. S12 of the Electronic Supplementary Information.

In conclusion, the achieved results for cation-anion RDFs showed that tail aggregation of the alkyl chain in non-polar domains is distinctively observed for ester-functionalized ILs with alkyl

side chain length longer than or equal to C_2, whereas larger alkyl linkage (at least C_4) is required

for the other series of ILs.[41-62] Thus, with the participation of ester group, the possibility of self-

assembly and micelle formation is enhanced which is in good agreement with experimental

finding of homologous ester functionalized ILs.[21]

3.2.5. Cation-cation interaction

Additional investigations of the bulk nanostructure properties and the incorporating effects of

ester functional group were gained by computing the site-site cation-cation RDFs. Accordingly,

the O_8 site of ester functional group was selected due to the concentration of negative charge.

Fig. 11 (a) indicates O_8-H_n RDFs of [$C_1COOC_4C_1im$][Br] ILs. Due to the similar pattern of O_8-

H_n RDFs, conforming results for the other selected ILs are shown in Figs. S13 to S15 of the

Electronic Supplementary Information. Both intra- and intermolecular interactions are

contributed to the cation-cation RDF diagram. The relative intensity of O_8-H_n RDFs increased

with lengthening the alkyl side chain of cation, clearly for the first peaks of O_8-H_{11} sites. It can

be simply understood that the larger peak of O_8-H_n RDFs is ascribed to the first peak of O_8-H_{11}

sites, which splits into two consecutive peaks. According to Fig. 12, this is the consequence of

intra- and intermolecular molecular H bonding formation between these sites. The first and

second peaks of O_8-H_{11} RDFs are centered at almost 2.5 Å and 3.8 Å, respectively. The second

peaks of O_8-H_n RDFs gradually vanish when alkyl side chain is lengthened. The other strong

interactions occurred via O_8-H_2 and O_8-H_5 sites within the 2-3 Å range. These findings are

comparable with the obtained results of *ab initio* calculations of the isolated ion pairs in our

earlier work[24], the average structures of cations (Figs. 3 and 4), and also with box analysis of

[$C_1COOC_4C_1im$][Br] IL (Fig. 12). Moreover, much weaker interactions between O_8-H_4, O_8-H_{10},

O_8-H_{12}, O_8-H_{13}, and O_8-H_{14} are centered at farther distances; 5, 6, 4.5, 5, and 7 Å, respectively.

The intensity of O_8-H_n RDFs decreased in the following manner: $[Tf_2N]^- > [TfO]^- > [PF_6]^- >$ $[BF_4]^- > [NO_3]^- \geq [Br]^-$. It may be related to the weaker cation-anion interactions of bulkier anions, which are replaced by cation-cation interactions. Eventually, the lowest cation-cation cohesion is formed via O_8-H_6 sites owing to more occupation in cation-anion interactions, which is previously proved by QTAIM analysis and *ab initio* results in earlier work.[24] Totally, the achieved results of O_8-H_n RDFs is in excellent agreement with the average structure of cation (Figs. 3 and 4) and bulk analysis of $[C_1COOC_4C_1im][Br]$ in the different locations of its simulation box (Fig. 12).

Fig. 11 (b) represents O_9-H_n RDFs for $[C_1COOC_4C_1im][Br]$ ILs. Due to the similar organization of H_n-O_9 sites, corresponding results for the other target ILs are plotted in Figs. S16 to S18 of the Electronic Supplementary Information. The strongest O_9-H_n interactions belong to O_9-H_{13} sites, followed by O_9-H_5, O_9-H_2, O_9-H_{14}, O_9-H_4, and O_9-H_{10}, respectively. The intensity of O_9-H_n RDFs are slightly raised when the alkyl side linkage of a cation is lengthened. Notably, O_9-H_{13} RDFs indicate two consecutive peaks, in which the first peak has significant lower amplitude (~2.5 Å) than the second one (~4 Å). The maximum intensity of the O_9-H_5, O_9-H_2, O_9-H_{14}, O_9-H_4, and O_9-H_{10} sites are located in the range of 4-5, 6-7, 4.5-5.5, and 7-8 Å, respectively. These findings are comparable with the optimized structures of isolated ion pair,[24] the average structures of cations, and the analysis of simulation box of $[C_1COOC_4C_1im][Br]$ IL in Figs. 13 and 14. The maximum intensity of H_n-O_9 RDFs becomes partially enhanced in the following order: $[Br]^- < [NO_3]^- < [BF_4]^- < [PF_6]^- < [TfO]^- < [Tf_2N]^-$, which is nearly similar to the observed trend for the first peaks of O_8-H_n RDFs. This may be explained by more involvement of the smaller anions with their cations, and less cation-anion association for weakly coordinating anions is compensated with strong cation-cation interactions. Among shown O_9-H_n RDFs, the

lowest interaction is attributed to the H_6 site, as previously seen for O_8-H_6 RDFs. Strong H_6-anion accompanied with unsuitable orientation of O_n and H_6 sites is assumed to be responsible for this observation. In general, the obtained results of O_9-H_n RDFs are in good consistency with the bulk analysis of $[C_1COOC_4C_1im][Br]$ in Figs. 13 and 14.

In addition, C_n-C_n RDFs between unlike C atoms of alkyl side chain for $[C_1COOC_4C_1im]$ cation are plotted in Fig. S20 of the Electronic Supplementary Information. Also, Fig. S21 of the Electronic Supplementary Information indicates C_2-C_2 as well as O_8-O_8 RDFs for these ILs. Likewise, anion-anion RDFs are depicted in Fig. S22 of the Electronic Supplementary Information.

3.2.6. Number of hydrogen bonds

Finally, the average numbers of hydrogen bonds ($\langle N_{HB} \rangle$) constituted from H_n-anion, O_8-H_n, and O_9-H_n interactions were computed, as follows:[66]

$$\langle N_{HB} \rangle = 4\pi\rho \int_0^{r_{min}} r^2 \, g(r) \, dr \tag{3}$$

where r_{min} is equal to 3 Å. As it can be observed from Table 4, the hydrogen bonds mainly formed via H_n-anion interaction, which is followed by O_8-H_n and O_9-H_n, respectively. The highest values of H_n-anion hydrogen bonds are attributed to the ester-functionalized cation paired with [Br] and $[NO_3]$. These interactions are replaced by O_8-H_n hydrogen bonds for ILs composed of poorly coordinating anions. Also, the strongest hydrogen bonds between cations belong to O_8 and H_{11} sites. According to the obtained results in Table 4, the possibility of hydrogen bond formation between O_8 and H_2 is higher than O_8-H_5, which is in good agreement with the gained results of torsion energy profiles in our earlier work.[24] The achieved results of torsion energy profiles in our previous study demonstrate that in the most stable conformer of cations, O_8-H_2 intra-molecular H bonds is significantly preferred.[24]

16

Additional structural features of target ILs were precisely gained by visualizing the tridimensional spatial distribution functions (SDFs) in Figs. S23 to S31.

4. SUMMARY AND CONCLUSIONS

The influences of ester functional group on nanostructural properties of biodegradable ILs composed of 3-methyl-1-(alkoxycarbonylmethyl) imidazolium cation ($[C_1COOC_nC_1im]^+$, n=1, 2, 4) paired with $[Br]^-$, $[NO_3]^-$, $[BF_4]^-$, $[PF_6]^-$, $[TfO]^-$, and $[Tf_2N]^-$ anions were explored by using the MD simulations and QTAIM method at 400 K. Nano-scale segregation analyses exhibit a small spherical hydrocarbon island-like formation within the continuous ionic domain for $[C_1COOC_1C_1im]$ ILs and sponge-like nanostructure for $[C_1COOC_4C_1im]$ ILs. In fact, ester-functionalized ILs with ethyl side ($[C_1COOC_2C_1im]$) are the turning point between two different morphologies. Segregation of polar and uncharged domains is more pronounced with lengthening alkyl side chain. Specifically, non-polar networks are observed for $[C_1COOC_4C_1im]$ ILs composed of smaller anions such as $[Br]$ and $[NO_3]$, whereas clustering organization is found for the other ILs. The possibility of micelle formation increased with elongation of the alkyl side chain length. This can be justified by the fact that head and ester groups along with their anions are homogeneously distributed owing to their similar net charges, whereas neutral tail groups tend to stay closer, with the equilibrium average distance decided only by their short-range interactions. Precisely, the distribution of cations with short alkyl side chain in the bulk phase is mostly determined by the charged head groups, where the tail groups do not have enough collective attractive energy to aggregate. Therefore, ions interact chaotically with one another. However, the interactions between tail groups become greater with lengthening alkyl side linkage due to the satisfaction of both requirements for segregation of the head and tail groups. In addition, $[C_1COOC_2C_1im]$ cation with a critical asymmetry, forms slight bicontinuous phase morphology from self-

assembly of polar and apolar groups in the bulk phase. Unexpectedly, the distinctive tail aggregation of the alkyl chains in non-polar domains can be found for ester functionalized ILs with alkyl side chain length longer than or equal to C_2, whereas larger alkyl linkage (at least C_4) is required for the other series of ILs. These results suggest that the incorporation of an ester group into the alkyl side chain of cation promotes the cation-anion interionic interactions, which subsequently results in stronger segregation between charged and apolar domains. As a result, the possibility of self-assembly and micelle formation is remarkably enhanced, which is in good agreement with experimental finding of homologous ILs. Moreover, the formation of O-H intra-molecular hydrogen bonding was extensively revealed from the achieved structural properties.

Electronic Supplementary Information (ESI) available: 1. A brief review of nanostructure organization in different series of ILs, 2. Force field parameters and MD details, 3. Quantum theory of atoms in molecule (QTAIM) analysis, 4. Electrostatic potential map (ESP), 5. Radial distribution functions (RDFs), 6. Spatial distribution functions (SDFs). See DOI: 10.1039/xxxxxxxxxx

AUTHOR INFORMATION

Corresponding Author

* E-mail: gholami@sharif.edu. Tel: +98 216 616 5314. Fax: +98 216 600 5718.

ACKNOWLEDGMENTS

References

(1)   T. L. Greaves and C. J. Drummond, *Chem. Soc. Rev.*, 2008, **37**, 1709-1726.

(2)   K. E. Gutowski and E. J. Maginn, *J. Am. Chem. Soc.*, 2008, **130**, 14690-14704.

(3)   G. Yu, S. Zhang, G. Zhou, X. Liu and X. Chen, *AIChE J.*, 2007, **53**, 3210-3221.

(4)   T. Welton, *Chem. Rev.*, 1999, **99** , 2071-2084

(5)   K. G., Sprenger, V. W. Jaeger and J. Pfaendtner, *J. Phys. Chem. B*, 2015, **119**, 5882-5895.

(6)   Y. Zhang and E. J. Maginn, *J. Phys. Chem. Lett.*, 2015, **6**, 700-705.

(7)   H. Liu and E. J. Maginn, *J. Chem. Phys.*, 2011, **135**, 124507-124522.

(8)   M. H. Kowsari and M. Fakhraee, *J. Chem. Eng. Data*, 2015, **60**, 551-560.

(9)   M. H. Kowsari, M. Fakhraee, S. Alavi and B. Najafi, *J. Chem. Eng. Data*, 2014, **59**, 2834-2849.

(10)   A. L. Revelli, F. Mutelet and J. N. Jaubert, *J. Phys. Chem. B*, 2010, **114**, 4600-4608.

(11)   A. Mondal and S. Balasubramanian, *J. Phys. Chem. B*, 2014, **118**, 3409-3422.

(12)   M. L. S. Batista, K. A. Kurnia, S. P. Pinho, J. R. B. Gomes and J. A. P. Coutinho, *J. Phys. Chem. B*, 2015, **119**, 1567-1578.

(13)   M. Fakhraee, B. Zandkarimi, H. Salari, M. R. Gholami, *J. Phys. Chem. B*, 2014, **118**, 14410-14428.

(14)   T. Mendez-Morales, J. Carrete, O. Cabeza, L. J. Gallego and L. M. Varela, *J. Phys. Chem. B*, 2011, **115**, 6995-7008.

(15)   Y. Tian, G. S. Goff, W. H. Runde and E. R. Batista, *J. Phys. Chem. B*, 2012, **116**, 11943-11952.

(16)   C. Kolbeck, I. Niedermaier, A. Deyko, K. R. J. Lovelock, N. Taccardi, W. Wei, P. Wasserscheid, F. Maier and H. P. Steinrück, *Chem. Eur. J.*, 2014, **20**, 3954-3965.

(17)   J. E. Bara, D. E. Camper, D. L. Gin and R. D. Noble, *Acc. Chem. Res.*, 2010, **43**, 152-159.

(18)   N. Gathergood, M. T. Garcia and P. J. Scammells, *Green Chem.*, 2004, **6**, 166-175.

(19)   M. T. Garcia, N. Gathergood and P. J. Scammells, *Green Chem.*, 2005, **7**, 9-14.

(20)   N. Gathergood, P. J. Scammells and M. T. Garcia, *Green Chem.*, 2006, **8**, 156-160.

(21)   M. T. Garcia, I. Ribosa, L. Perez, A. Manresa and F. Comelles, *Langmuir*, 2013, **29**, 2536-2545.

(22)   G. Singh and T. S. Kang, *J. Phys. Chem. B*, 2015, **119**, 10573-10585.

(23)   H. Gui, Y. Li, S. Chen, P. Xu, B. Zheng and Y. Ding, *Macromolecular Research*, 2014, **22**, 583-591.

(24)   M. Fakhraee and M. R. Gholami, *Ind. Eng. Chem. Res.*, 2015, **54**, 11678–11700A. S. Pensado, A. A. H. Pádua a*nd M. F. Costa Gomes*, *J. Phys. Chem. B*, 2011, **115**, 3942-3948.

(25)   M. J. Frisch, G. W. Trucks, H. B. Schlegel, G. E. Scuseria, M. A. Robb, J. R. Cheeseman, J. A. Montgomery, Jr., T. Vreven, K. N. Kudin, J. C. Burant, J. M. Millam, S. S. Iyengar, J. Tomasi, V. Barone, B. Mennucci, M. Cossi, G. Scalmani, N. Rega, G. A. Petersson, H. Nakatsuji, M. Hada, M. Ehara, K. Toyota, R. Fukuda, J. Hasegawa, M. Ishida, T. Nakajima, Y. Honda, O. Kitao, H. Nakai, M. Klene, X. Li, J. E. Knox, H. P. Hratchian, J. B. Cross, V. Bakken, C. Adamo, J. Jaramillo, R. Gomperts, R. E. Stratmann, O. Yazyev, A. J. Austin, R. Cammi, C. Pomelli, J. W. Ochterski, P. Y. Ayala, K. Morokuma, G. A. Voth, P. Salvador, J. J. Dannenberg, V. G. Zakrzewski, S. Dapprich, A. D. Daniels, M. C. Strain, O. Farkas, D. K. Malick, A. D. Rabuck, K. Raghavachari, J. B. Foresman, J. V. Ortiz, Q. Cui, A. G. Baboul, S. Clifford, J.

Cioslowski, B. B. Stefanov, G. Liu, A. Liashenko, P. Piskorz, I. Komaromi, R. L. Martin, D. J. Fox, T. Keith, M. A. Al-Laham, C. Y. Peng, A. Nanayakkara, M. Challacombe, P. M. W. Gill, B. Johnson, W. Chen, M. W. Wong, C. Gonzalez and J. A. Pople, *Gaussian 03, Revision C.02*; Gaussian, Inc.: Wallingford, CT, 2004.

(26)   R. F. W. Bader, *Atom in Molecules: A Quantum Theory*; Oxford University Press: New York, 1990.

(27)   T. Lu and F. Chen, *J. Comput. Chem.*, 2012, **33**, 580-592.

(28)   H. Gao, Y. Zhang, H. J. Wang, J. Liu and J. Chen, *J. Phys. Chem. A*, 2010, **114**, 10243-10252.

(29)   Y. Gao, H. Q. Wu, R. L. Zhong, H. L. Xu, S. L. Sun, L. Zhao and Z. M. Su, *Int. J. Quant. Chem.*, 2014, **114**, 1692-1696.

(30)   M. Izadyar, M. Khavani and M. R. Housaindokht, *Phys. Chem. Chem. Phys.*, 2015, **17**, 11382-11391.

(31)   A. Mohajeri, and A. Ashrafi, *J. Phys. Chem. A*, 2011, **115**, 6589-6593.

(32)   A. Shurki, P. C. Hiberty and S. Shaik, *J. Am. Chem. Soc.*, 1999, **121**, 822-834.

(33)   A. D. Becke and K. E. Edgecombe, *J. Chem. Phys.*, 1990, **92**, 5397-5403.

(34)   T. Lu and F. W. Chen, *Acta Physico-Chimica Sinica*, 2011, **27**, 2786-2792.

(35)   A. Savin, O. Jepsen, J. Flad, O. K. Andersen, H. Preuss and H. G. Schnering, *Angew. Chem. Int. Ed. Engl.*, 1992, **31**, 187-188.

(36)   H. L. Schmider and A. D. Becke, *J. Mol. Struct.*, 2000, **527**, 51-61.

(37)   R. P. Matthews, C. Ashworth, T. Welton and P. A. Hunt, *J. Phys.: Condens. Matter*, 2014, **26**, 284112.

(38)   P. A. Hunt, C. R. Ashworth, and R. P. Matthews, *Chem. Soc. Rev.*, 2015, **44**, 1257-1288.

(39)　B. A. Marekha, O. N. Kalugin and A. Idrissi, *Phys. Chem. Chem. Phys.*, 2015, **17**, 16846-16857.

(40)　W. Beichel, N. Trapp, C. Hauf, O. Kohler, G. Eickerling, W. Scherer and I. Krossing, *Angew. Chem. Int . Ed.*, 2014, **53**, 3143–3146.

(41)　J. N. A. Canongia Lopes and A. A. H. Pádua, *J. Phys. Chem. B*, 2006, **110**, 3330-3335.

(42)　A. A. H. Pádua, M. F. C. Gomes, J. N. A. Canongia Lopes, *Acc. Chem. Res.*, 2007, **40**, 1087-1096.

(43)　C. J. Margulis, *Mol. Phys.*, 2004, **102**, 829-838.

(44)　Y. Wang, and G. A. Voth, *J. Am. Chem. Soc.*, 2005, **127**, 12192-12193.

(45)　S. Tsuzuki, W. Shinoda, H. Saito, M. Mikami, H. Tokuda and M. Watanabe, *J. Phys. Chem. B*, 2009, **113**, 10641-10649.

(46)　K. Shimizu, A. A. H. Pádua and J. N. Canongia Lopes, *J. Phys. Chem. B*, 2010, **114**, 15635-15641.

(47)　T. Pott and P. Méléard, *Phys. Chem. Chem. Phys.*, 2009, **11**, 5469-5475.

(48)　T. L. Greaves, D. F. Kennedy, S. T. Mudie and C. J. Drummond, *J. Phys. Chem. B*, 2010, **114**, 10022-10031.

(49)　O. Russina, L. Gontrani, B. Fazio, D. Lombardo, A. Triolo and R. Caminiti, *Chem. Phys. Lett.*, 2010, **493**, 259-262.

(50)　O. Russina, A. Triolo, L.; Gontrani and R. Caminiti, *J. Phys. Chem. Lett.*, 2012, **3**, 27-33.

(51)　O. Russina, A. Triolo, L. Gontrani, R. Caminiti, D. Xiao, L. G. Hines, R. A. Bartsch, E. L. Quitevis, N. Plechkova and K. R. Seddon, *J. Phys.: Condens. Matter*, 2009, **21**, 424121-424129.

(52)   A. Triolo, O. Russina, H.-J. Bleif and E. Di Cola, *J. Phys. Chem. B*, 2007, **111**, 4641-4644.

(53)   A. Triolo, O. Russina, B. Fazio, R. Triolo and E. Di Cola, *Chem. Phys. Lett.*, 2008, **457**, 362-365.

(54)   X. Paredes, J. Fernández, A. A. H. Pádua, P. Malfreyt, F. Malberg, B. Kirchner and A. S. Pensado, *J. Phys. Chem. B*, 2012, **116**, 14159-14170.

(55)   S. Yeganegi, A. Soltanabadi and D. Farmanzadeh, *J. Phys. Chem. B*, 2012, **116**, 11517-11526.

(56)   Y. Shen, D. F. Kennedy, T. L. Greaves, A. Weerawardena, R. J. Mulder, N. Kirby, G. Song and C. J. Drummonda, *Phys. Chem. Chem. Phys.*, 2012, **14**, 7981-7992.

(57)   S. Li, G. Feng, J. L. Bañuelos, G. Rother, P. F. Fulvio, S. Dai and P. T. Cummings, *J. Phys. Chem. C*, 2013, **117**, 18251-18257.

(58)   A. A. Freitas, K. Shimizu and J. N. Canongia Lopes, *J. Chem. Eng. Data*, 2014, **59**, 3120-3129.

(59)   K. Shimizu, C. E. S. Bernardes and J. N. Canongia Lopes, *J. Phys. Chem. B*, 2014, **118**, 567-576.

(60)   K. Wei, L. Deng, Y. Wang, Z. Ou-Yang and G. Wang, *J. Phys. Chem. B*, 2014, **118**, 3642-3649.

(61)   R. Hayes, S. Imberti, G. G. Warr and R. Atkin, *J. Phys. Chem. C*, 2014, **118**, 13998-14008.

(62)   R. Hayes, G. G. Warr and R. Atkin, *Chem. Rev.*, 2015, **115**, 6357-6426.

(63)   H. Weber, O. Hollóczki, A. S. Pensado and B. Kirchner, *J. Chem. Phys.*, 2013, **139**, 084502.

(64)   E. Bodo, M. Chiricotto and R. Caminiti, *J. Phys. Chem. B*, 2011, **115**, 14341-14347.

(65)   M. Brehm and B. Kirchner, *J. Chem. Inf. Model.*, 2011, **51**, 2007-2023.

(66)   S. Alavi, K. Shin and J. A. Ripmeester, *J. Chem. Eng. Data*, 2015, **60**, 389-397.

Table 1. Topological properties for the interionic interactions at the BCPs of $[C_1COOC_1C_1im][anion]_3$ ILs composed of [Br], [NO$_3$], and [BF$_4$] anions, calculated at the B3LYP/6-311++G(d,p) level. Indexes correspond to specified labels in Fig. 2.

$[C_1COOC_1C_1im][Br]_3$	ρ_b	$\nabla^2\rho_b$	G_b	V_b	$-G_b/V_b$	H_b	ELF	LOL
1	0.00414	0.01037	0.00212	-0.00165	1.28485	0.00047	0.02023	0.12618
2	0.01922	0.04643	0.01048	-0.00936	1.11966	0.00112	0.12468	0.27419
3	0.01372	0.03444	0.00730	-0.00599	1.21869	0.00131	0.08711	0.23625
4	0.00712	0.01761	0.00362	-0.00284	1.27465	0.00078	0.04161	0.17283
5	0.00915	0.02346	0.00482	-0.00377	1.27851	0.00105	0.05357	0.19251
6	0.01456	0.03593	0.00770	-0.00642	1.19938	0.00128	0.09456	0.24447
$[C_1COOC_1C_1im][NO_3]_3$	ρ_b	$\nabla^2\rho_b$	G_b	V_b	$-G_b/V_b$	H_b	ELF	LOL
1	0.01251	0.04158	0.00887	-0.00735	1.20680	0.00152	0.04533	0.17908
2	0.02458	0.08261	0.01856	-0.01648	1.12621	0.00208	0.09357	0.24326
3	0.01640	0.05231	0.01141	-0.00976	1.16906	0.00165	0.06611	0.21029
4	0.01463	0.04993	0.01056	-0.00864	1.22222	0.00192	0.05347	0.19218
5	0.01288	0.04144	0.00890	-0.00745	1.19463	0.00145	0.04946	0.18592
6	0.01603	0.05027	0.01103	-0.00951	1.15983	0.00152	0.06561	0.20962
$[C_1COOC_1C_1im][BF_4]_3$	ρ_b	$\nabla^2\rho_b$	G_b	V_b	$-G_b/V_b$	H_b	ELF	LOL
1	0.01144	0.04325	0.00935	-0.00789	1.18504	0.00146	0.03071	0.15124
2	0.01098	0.04278	0.00916	-0.00763	1.20052	0.00153	0.02799	0.14520
3	0.01749	0.06637	0.01469	-0.01275	1.15216	0.00194	0.05031	0.18720
4	0.00380	0.01559	0.00314	-0.00238	1.31933	0.00076	0.00710	0.07819
5	0.00796	0.02869	0.00617	-0.00518	1.19112	0.00099	0.02128	0.12867
6	0.00887	0.03156	0.00684	-0.00580	1.17931	0.00104	0.02477	0.13764
7	0.01419	0.05391	0.01167	-0.00987	1.18237	0.00180	0.04013	0.16988
8	0.01415	0.05315	0.01151	-0.00972	1.18416	0.00179	0.04088	0.17124
9	0.01422	0.05060	0.01122	-0.00979	1.14607	0.00143	0.04351	0.17592
10	0.00779	0.02963	0.00635	-0.00529	1.20038	0.00106	0.01873	0.12156

Table 2. Topological properties for the interionic interactions at the BCPs of [C$_1$COOC$_1$C$_1$im][anion]$_3$ ILs composed of [PF$_6$], [TfO], and [Tf$_2$N] anions, calculated at the B3LYP/6-311++G(d,p) level. Indexes correspond to specified labels in Fig. 2.

[C$_1$COOC$_1$C$_1$im][PF$_6$]$_3$	ρ_b	$\nabla^2\rho_b$	G_b	V_b	$-G_b/V_b$	H_b	ELF	LOL
1	0.00978	0.03789	0.00816	-0.00685	1.19124	0.00131	0.02411	0.13598
2	0.01122	0.04394	0.00942	-0.00786	1.19847	0.00156	0.02846	0.14625
3	0.01600	0.06203	0.01361	-0.01171	1.16225	0.00190	0.04388	0.17654
4	0.00392	0.01652	0.00335	-0.00257	1.30350	0.00078	0.00689	0.07713
5	0.00784	0.02916	0.00627	-0.00524	1.19657	0.00103	0.01968	0.12426
6	0.00918	0.03363	0.00730	-0.00620	1.17742	0.00110	0.02432	0.13651
7	0.01243	0.04891	0.01048	-0.00873	1.20046	0.00175	0.03229	0.15459
8	0.01291	0.04994	0.01072	-0.00895	1.19777	0.00177	0.03489	0.15988
9	0.01337	0.04916	0.01083	-0.00936	1.15705	0.00147	0.03830	0.16649
10	0.00615	0.02605	0.00547	-0.00443	1.23476	0.00104	0.01159	0.09788
[C$_1$COOC$_1$C$_1$im][TfO]$_3$	ρ_b	$\nabla^2\rho_b$	G_b	V_b	$-G_b/V_b$	H_b	ELF	LOL
1	0.01324	0.04539	0.00966	-0.00798	1.21053	0.00168	0.04622	0.18057
2	0.02187	0.07803	0.01712	-0.01474	1.16147	0.00238	0.07595	0.22291
3	0.01232	0.03918	0.00856	-0.00732	1.18560	0.00134	0.04630	0.18073
4	0.01428	0.05208	0.01088	-0.00873	1.24628	0.00215	0.04685	0.18160
5	0.01372	0.04807	0.01015	-0.00829	1.22437	0.00186	0.04701	0.18189
6	0.01069	0.03265	0.00715	-0.00613	1.16639	0.00102	0.04147	0.17239
[C$_1$COOC$_1$C$_1$im][Tf$_2$N]$_3$	ρ_b	$\nabla^2\rho_b$	G_b	V_b	$-G_b/V_b$	H_b	ELF	LOL
1	0.01355	0.04806	0.01014	-0.00826	1.22760	0.00188	0.04530	0.17901
2	0.01857	0.06096	0.01298	-0.01073	1.20969	0.00225	0.07642	0.22353
3	0.00942	0.03145	0.00671	-0.00555	1.20901	0.00116	0.03125	0.15244
4	0.00876	0.02559	0.00547	-0.00453	1.24724	0.00112	0.03669	0.16353
5	0.01498	0.05665	0.01175	-0.00933	1.25938	0.00242	0.04712	0.18204
6	0.01086	0.04031	0.00834	-0.00659	1.26555	0.00175	0.03244	0.15493
7	0.00975	0.03403	0.00724	-0.00596	1.21477	0.00128	0.03010	0.14996
8	0.00637	0.01976	0.00421	-0.00348	1.20977	0.00073	0.02174	0.13000
9	0.00553	0.01819	0.00391	-0.00327	1.19572	0.00064	0.01590	0.11303

Table 3. Characteristic parameters of RDFs such as location of their first maximum (max_1) and minimum (min_1) alongside their coordination number in the first shell (N).

$[C_1COOC_1C_1im]$	max_1^*	min_1^*	N^*	$max_1^\ddagger$	$min_1^\ddagger$	$N^\ddagger$	$max_1^\dagger$	$min_1^\dagger$	$N^\dagger$
[Br]	3.5750	6.6250	2.14	4.2933	5.9466	1.42	3.8750	5.3750	2.04
$[NO_3]$	3.6250	6.8750	2.23	4.1333	5.6266	1.55	3.8750	5.3750	2.09
$[BF_4]$	3.9250	7.3250	2.16	4.5600	6.1066	1.49	3.9250	5.4250	1.90
$[PF_6]$	4.2250	7.5750	2.10	4.9333	6.4800	1.53	3.8750	5.6250	1.86
[TfO]	3.9250	7.3750	2.00	4.9866	6.5330	1.49	3.9250	5.4750	1.85
$[Tf_2N]$	5.4250	8.7250	2.00	5.2000	7.3333	1.45	3.9250	5.6750	1.70
$[C_1COOC_2C_1im]$	max_1^*	min_1^*	N^*	$max_1^\ddagger$	$min_1^\ddagger$	$N^\ddagger$	$max_1^\dagger$	$min_1^\dagger$	$N^\dagger$
[Br]	3.5750	6.6250	2.03	4.2933	5.6800	1.31	4.0250	6.3250	2.45
$[NO_3]$	3.6250	6.8750	2.11	4.1333	5.8400	1.38	3.9750	6.2750	2.52
$[BF_4]$	3.8750	7.3250	2.05	4.6133	6.1066	1.35	4.0250	6.3250	2.32
$[PF_6]$	4.2250	7.6750	2.00	4.9866	6.5866	1.41	4.0250	6.3750	2.12
[TfO]	3.9250	7.3750	1.90	4.9333	6.5333	1.35	4.0250	6.4750	2.23
$[Tf_2N]$	5.3750	8.7750	1.91	5.2000	7.1733	1.28	4.0250	6.6750	1.98
$[C_1COOC_4C_1im]$	max_1^*	min_1^*	N^*	$max_1^\ddagger$	$min_1^\ddagger$	$N^\ddagger$	$max_1^\dagger$	$min_1^\dagger$	$N^\dagger$
[Br]	3.5750	6.6750	1.96	4.3466	6.0533	1.25	4.1250	7.0250	2.78
$[NO_3]$	3.6250	6.9750	2.04	4.2933	6.3733	1.41	4.0750	7.1250	3.00
$[BF_4]$	3.8750	7.3250	1.95	4.5600	6.6400	1.36	4.1250	7.2250	2.87
$[PF_6]$	4.2250	7.6750	1.89	5.2533	6.9066	1.36	4.1250	7.0750	2.53
[TfO]	3.8750	7.3750	1.85	4.6666	6.8000	1.27	4.1250	7.4250	2.79
$[Tf_2N]$	5.3750	8.7250	2.14	5.1466	7.7066	1.56	5.1750	7.7750	2.58

* Correspond to C_2-anion RDFs in Fig. 10 (a).

‡ Correspond to cation-anion center-of-mass RDFs in Fig. 10 (b).

† Correspond to terminal carbon atoms RDFs (C_{11}-C_{11}, C_{12}-C_{12}, C_{14}-C_{14}) in Fig. 7.

Table 4. Average number of hydrogen bond calculated from RDFs peaks.

$[C_1COOC_1C_1im]$	H_2-a[*]	H_4-a[*]	H_5-a[*]	H_6-a[*]	H_{10}-a[*]	O_8-H_2[†]	O_8-H_5[†]	O_8-H_{11}[†]	O_9-H_{13}[‡]
[Br]	0.53	0.47	0.47	0.34	0.26	0.22	0.18	0.52	--
$[NO_3]$	0.45	0.39	0.40	0.35	0.32	0.24	0.21	0.53	--
$[BF_4]$	0.31	0.27	0.28	0.24	0.23	0.21	0.21	0.49	--
$[PF_6]$	0.23	0.20	0.20	0.17	0.17	0.23	0.19	0.47	--
[TfO]	0.35	0.27	0.29	0.25	0.22	0.23	0.18	0.49	--
$[Tf_2N]$	0.22	0.16	0.18	0.17	0.15	0.22	0.17	0.45	--
$[C_1COOC_2C_1im]$	H_2-A[*]	H_4-A[*]	H_5-A[*]	H_6-A[*]	H_{10}-A[*]	O_8-H_2[†]	O_8-H_5[†]	O_8-H_{11}[†]	O_9-H_{13}[‡]
[Br]	0.53	0.47	0.49	0.34	0.26	0.21	0.19	0.65	--
$[NO_3]$	0.45	0.38	0.39	0.33	0.32	0.24	0.20	0.64	--
$[BF_4]$	0.32	0.26	0.27	0.23	0.22	0.23	0.19	0.61	--
$[PF_6]$	0.23	0.20	0.20	0.17	0.17	0.24	0.19	0.61	--
[TfO]	0.36	0.27	0.29	0.24	0.22	0.23	0.18	0.61	--
$[Tf_2N]$	0.22	0.17	0.18	0.16	0.15	0.23	0.16	0.59	--
$[C_1COOC_4C_1im]$	H_2-A[*]	H_4-A[*]	H_5-A[*]	H_6-A[*]	H_{10}-A[*]	O_8-H_2[†]	O_8-H_5[†]	O_8-H_{11}[†]	O_9-H_{13}[‡]
[Br]	0.55	0.48	0.49	0.34	0.26	0.20	0.15	0.60	0.08
$[NO_3]$	0.44	0.38	0.38	0.32	0.32	0.23	0.17	0.59	0.07
$[BF_4]$	0.32	0.26	0.27	0.22	0.22	0.22	0.17	0.60	0.06
$[PF_6]$	0.23	0.19	0.20	0.16	0.16	0.21	0.17	0.58	0.05
[TfO]	0.36	0.27	0.29	0.24	0.23	0.21	0.19	0.59	0.05
$[Tf_2N]$	0.27	0.27	0.21	0.19	0.17	0.27	0.20	0.69	0.05

* Correspond to H_n-anion RDFs in Figs. S8 to S10 of Electronic Supplementary Information

‡ Correspond to O_8-H_n RDFs in Figs. S13 to S15 of Electronic Supplementary Information.

† Correspond to terminal O_9-H_n RDFs Figs. S16 to S18 of Electronic Supplementary Information.

Figure Captions

Figure 1. (Online color) Ball and stick model of ester-functionalized ILs in this study along with their labels.

Figure 2. (Online color) BCPs (in orange color), CCPs (in yellow color), and RCPs (in yellow color) of optimized configurations of $[C_1COOC_1C_1im][anion]_3$ ILs, computed at the B3LYP/6-311++G(d,p) theoretical level.

Figure 3. (Online color) The average structures of $[C_1COOC_nC_1im]$ cations in the equilibrated simulation boxes gained from MD simulations at 400 K. The H bonds of O_8-H_n are shown by dotted line, and distances are in Å.

Figure 4. (Online color) The average structures of $[C_1COOC_nC_1im]$ cations in the equilibrated simulation boxes obtanied from MD simulations at 400 K. The H bonds of O_9-H_n are shown by dotted line, and distances are in Å.

Figure 5. (Online color) Snapshots of equilibrated simulation boxes of $[C_1COOC_nC_1im]$ ILs paired with [Br], $[NO_3]$, and $[BF_4]$ at 400 K. Green/red coloring code scheme was implemented for revealing the polar- (in red color) and non polar domains (in green color).

Figure 6. (Online color) Snapshots of equilibrated simulation boxes of $[C_1COOC_nC_1im]$ ILs paired with $[PF_6]$, [TfO], and $[Tf_2N]$ at 400 K. The green/red coloring code scheme was utilized for disclosing the polar- (in red color) and non polar domains (in green color).

Figure 7. (Online color) Site-site cation-cation RDFs between the terminal carbon atoms of the alkyl side chain (C_n-C_n) of $[C_1COOC_nC_1im]$ cations at 400 K.

Figure 8. (Online color) Micelle-like nanostructure of the equilibrated simulation boxes of $[C_1COOC_nC_1im][Br]$ ILs at 400 K.

Figure 9. (Online color) Micelle-like nanostructure of the equilibrated simulation box of $[C_1COOC_4C_1im][Br]$ ILs in high resolution at 400 K.

Figure 10 (Online color) (a) C_2-anion RDFs of $[C_1COOC_4C_1im][Br]$ IL at 400 K. (b) Cation-anion center-of-mass RDFs of $[C_1COOC_4C_1im][Br]$ IL at 400 K. (c) H_n-anion RDFs of $[C_1COOC_4C_1im][Br]$ IL at 400 K.

Figure 11. (Online color) (a) O_8-H_n RDFs of $[C_1COOC_4C_1im][NO_3]$ IL at 400 K. (b) O_9-H_n RDFs of $[C_1COOC_4C_1im][Br]$ IL at 400 K.

Figure 12. (Online color) Selected snapshots from the different parts of the equilibrated simulation box of $[C_1COOC_4C_1im][Br]$ at 400 K. The H bonds of O_8-H_n (n= 2, 5, 11, 12) are shown by dotted line, and distances are in Å.

Figure 13. (Online color) Selected snapshots from the different parts of the equilibrated simulation box of $[C_1COOC_4C_1im][Br]$ at 400 K. The H bonds of O_9-H_n (n= 2, 4, 5) are shown by dotted line, and distances are in Å.

Figure 14. (Online color) Selected snapshots from the different parts of the equilibrated simulation box of $[C_1COOC_4C_1im][Br]$ at 400 K. The H bonds of O_9-H_n (n= 13, 14) are shown by dotted line, and distances are in Å.
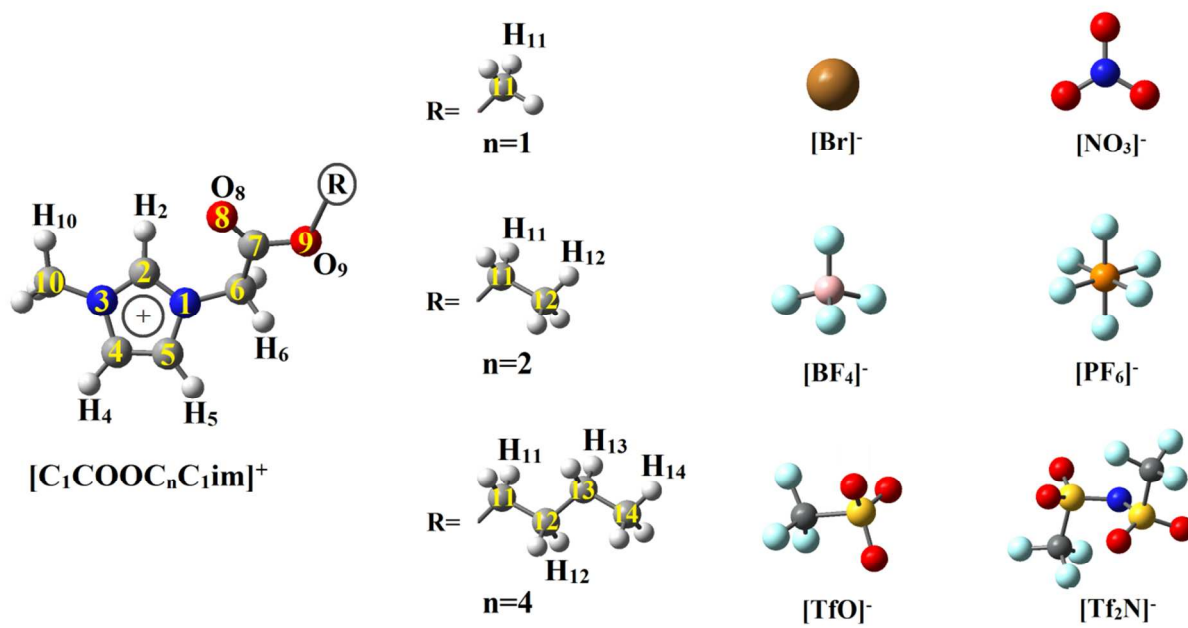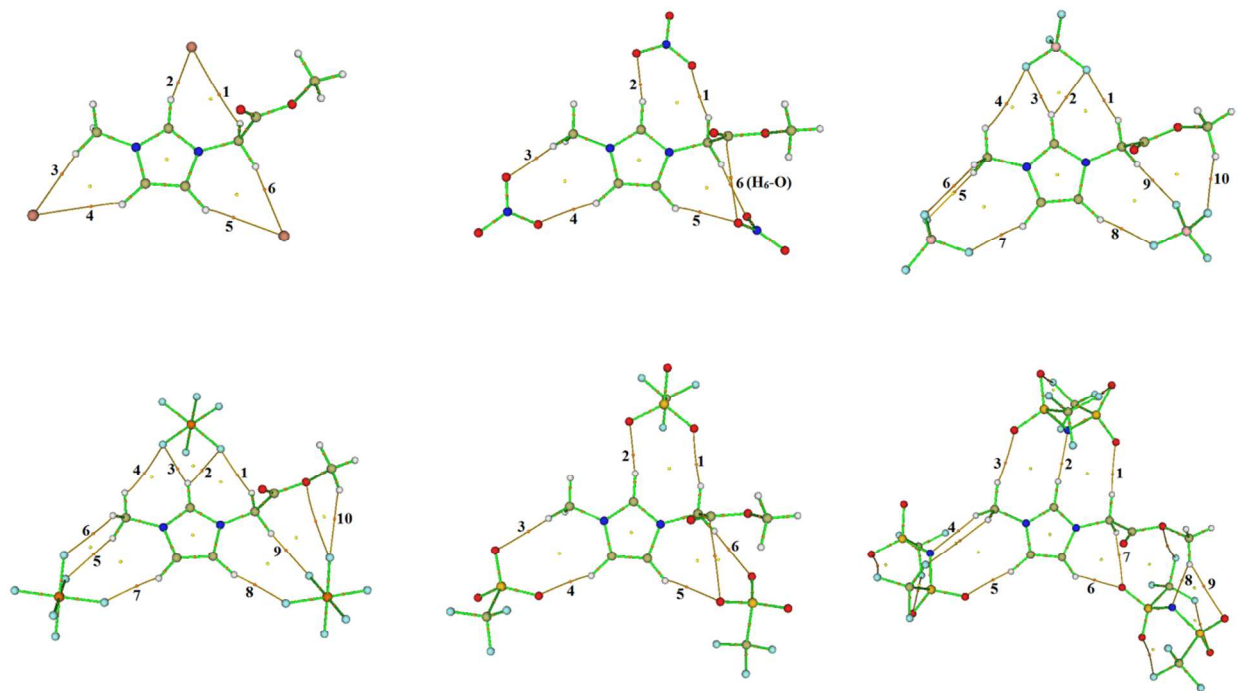
Figure 1.

Figure 2.

Figure 3.

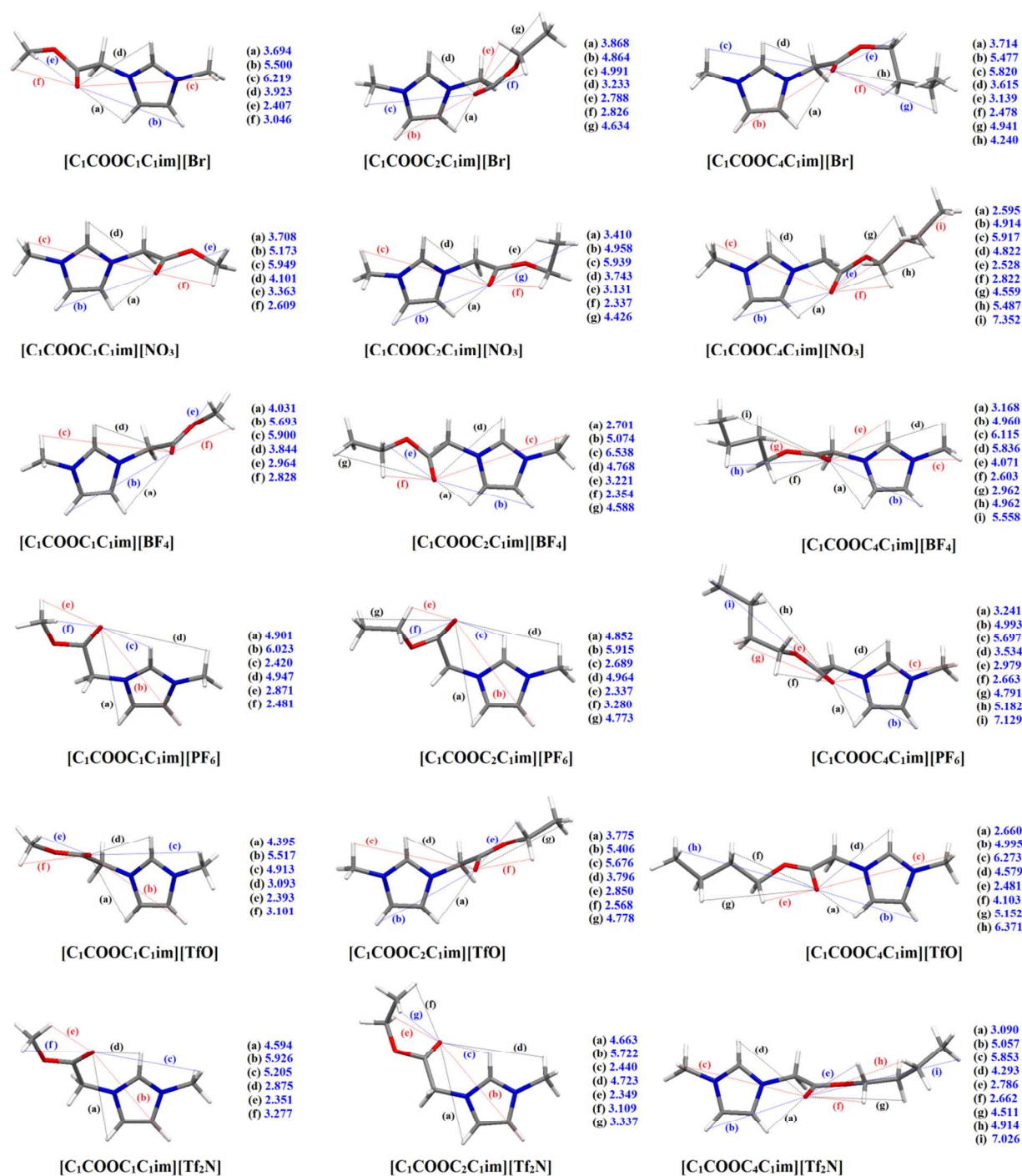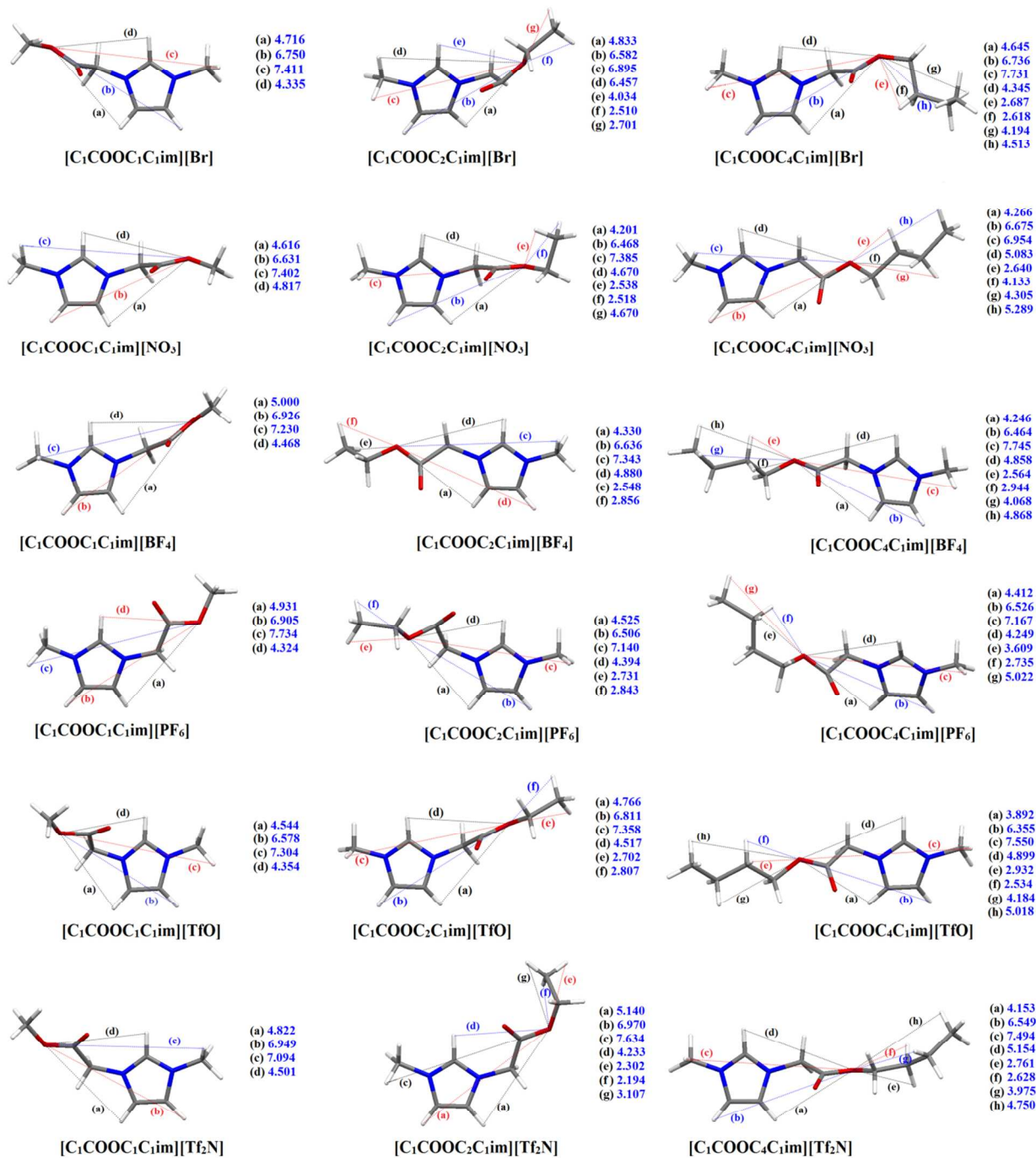**Figure 4.**

$[C_1COOC_1C_1im][Br]$ $[C_1COOC_2C_1im][Br]$ $[C_1COOC_4C_1im][Br]$

$[C_1COOC_1C_1im][NO_3]$ $[C_1COOC_2C_1im][NO_3]$ $[C_1COOC_4C_1im][NO_3]$

$[C_1COOC_1C_1im][BF_4]$ $[C_1COOC_2C_1im][BF_4]$ $[C_1COOC_4C_1im][BF_4]$

Figure 5.

[C₁COOC₁C₁im][PF₆] [C₁COOC₂C₁im][PF₆] [C₁COOC₄C₁im][PF₆]

[C₁COOC₁C₁im][TfO] [C₁COOC₂C₁im][TfO] [C₁COOC₄C₁im][TfO]

[C₁COOC₁C₁im][Tf₂N] [C₁COOC₂C₁im][Tf₂N] [C₁COOC₄C₁im][Tf₂N]

Figure 6.

Figure 7.

[C₁COOC₁C₁im][Br]

[C₁COOC₂C₁im][Br]

[C₁COOC₄C₁im][Br]

Figure 8.

[C₁COOC₄C₁im][Br]
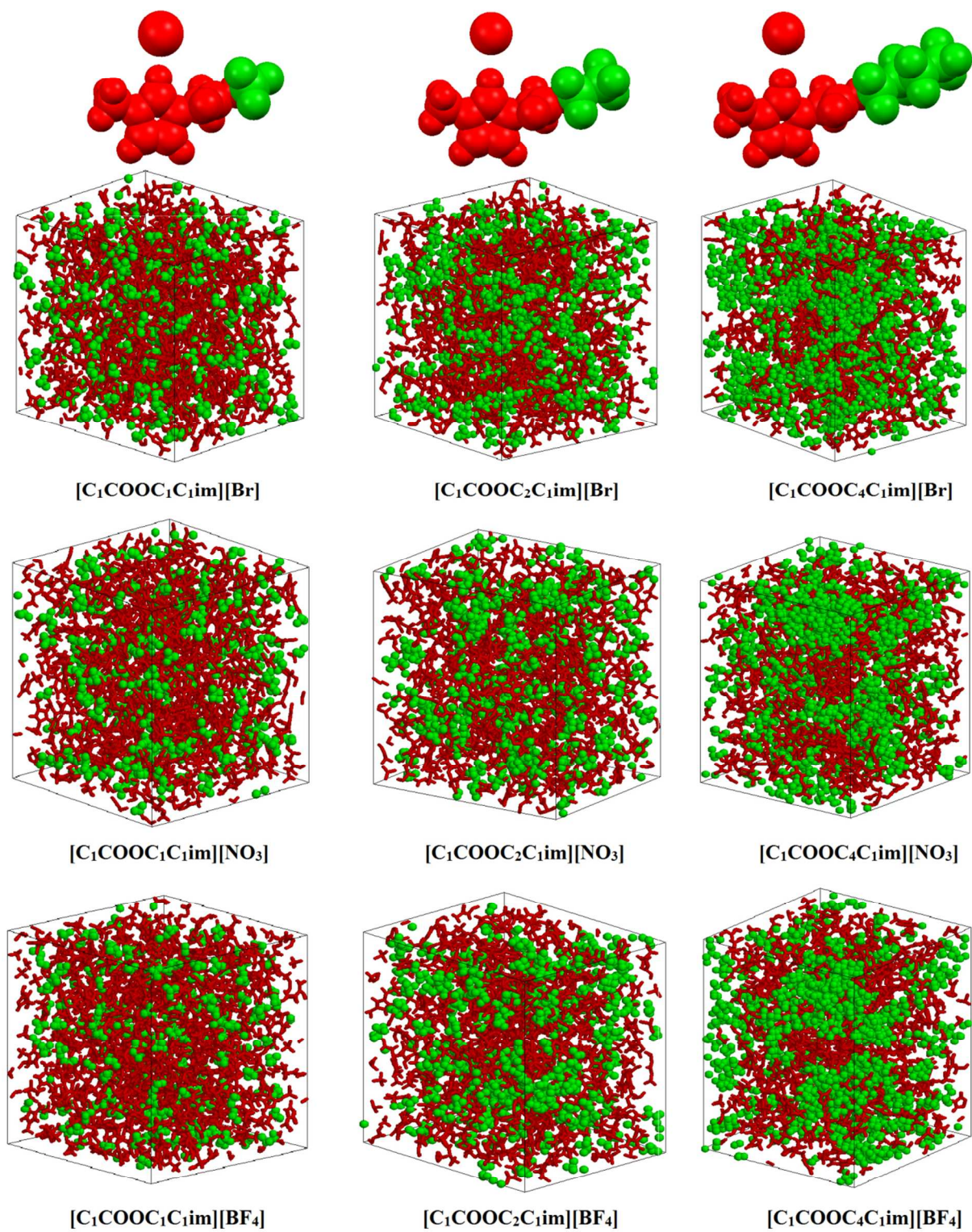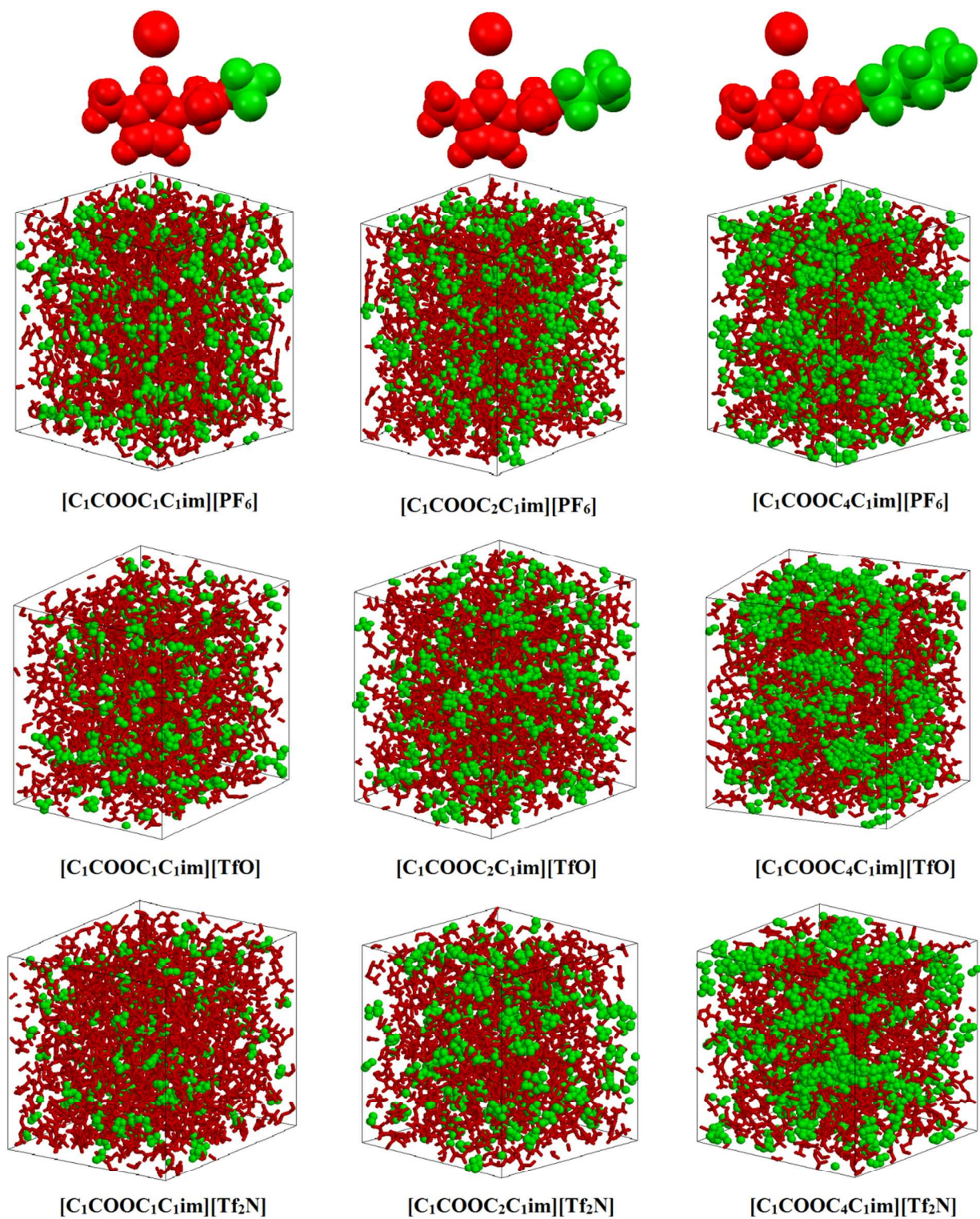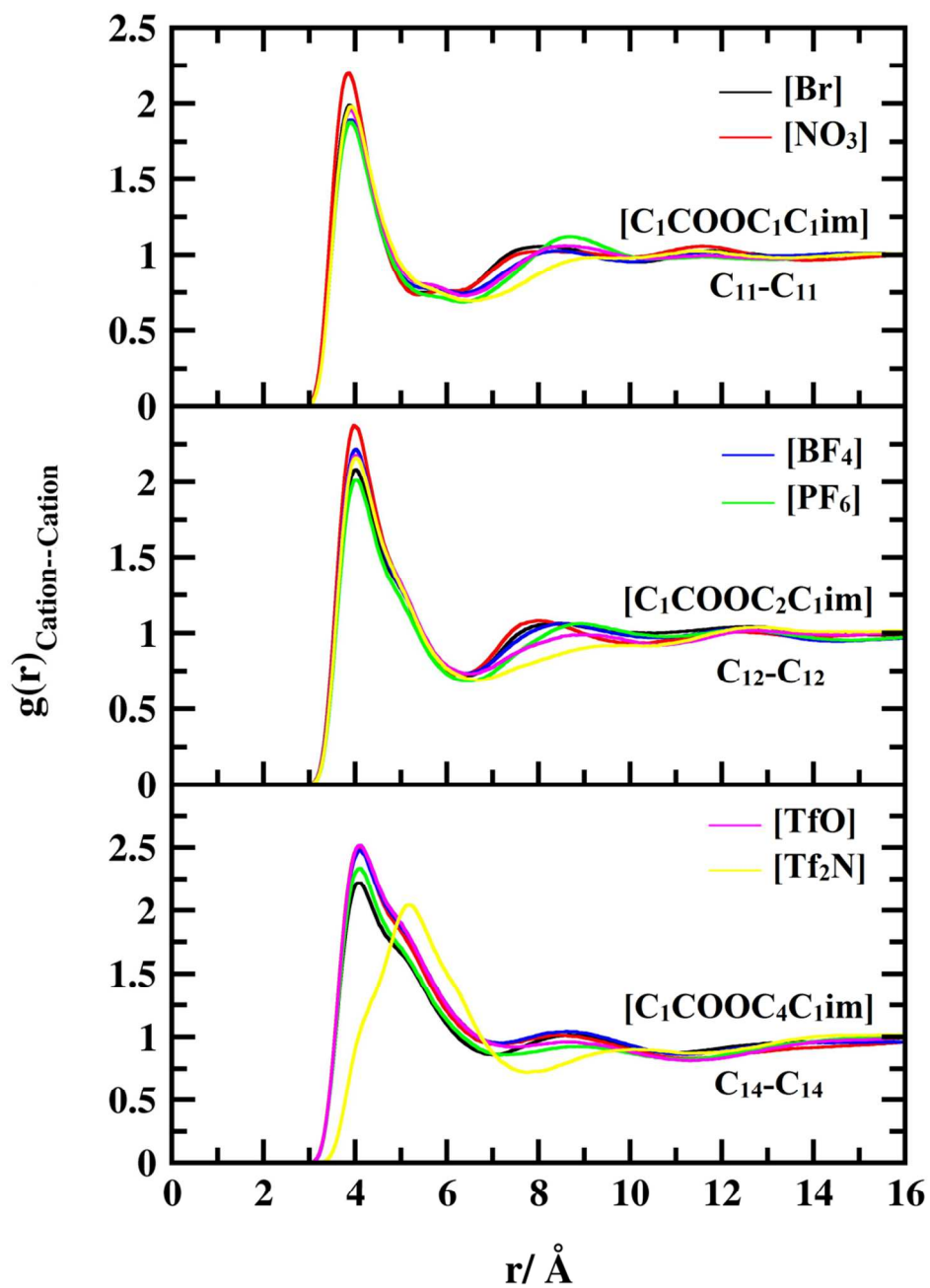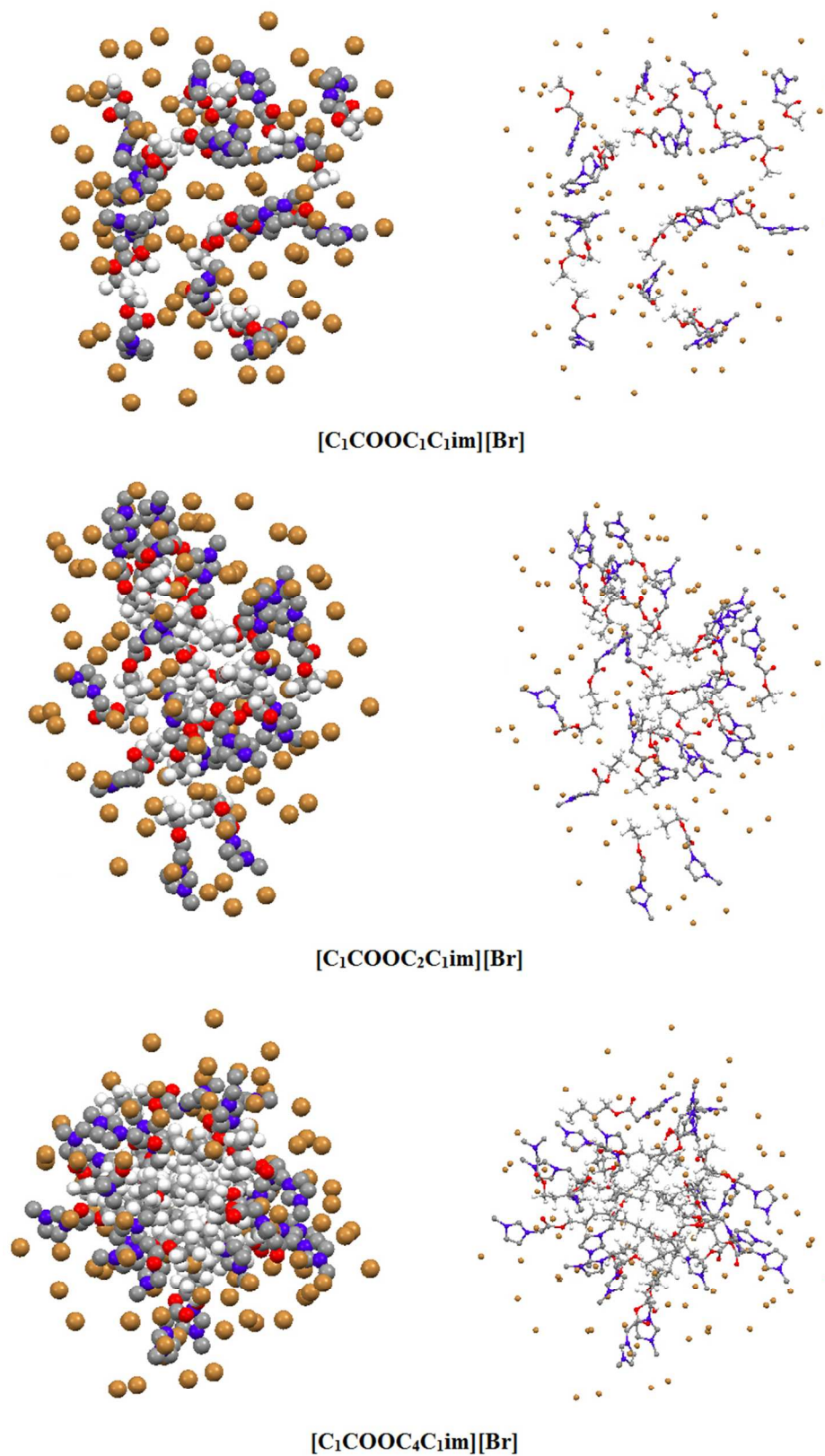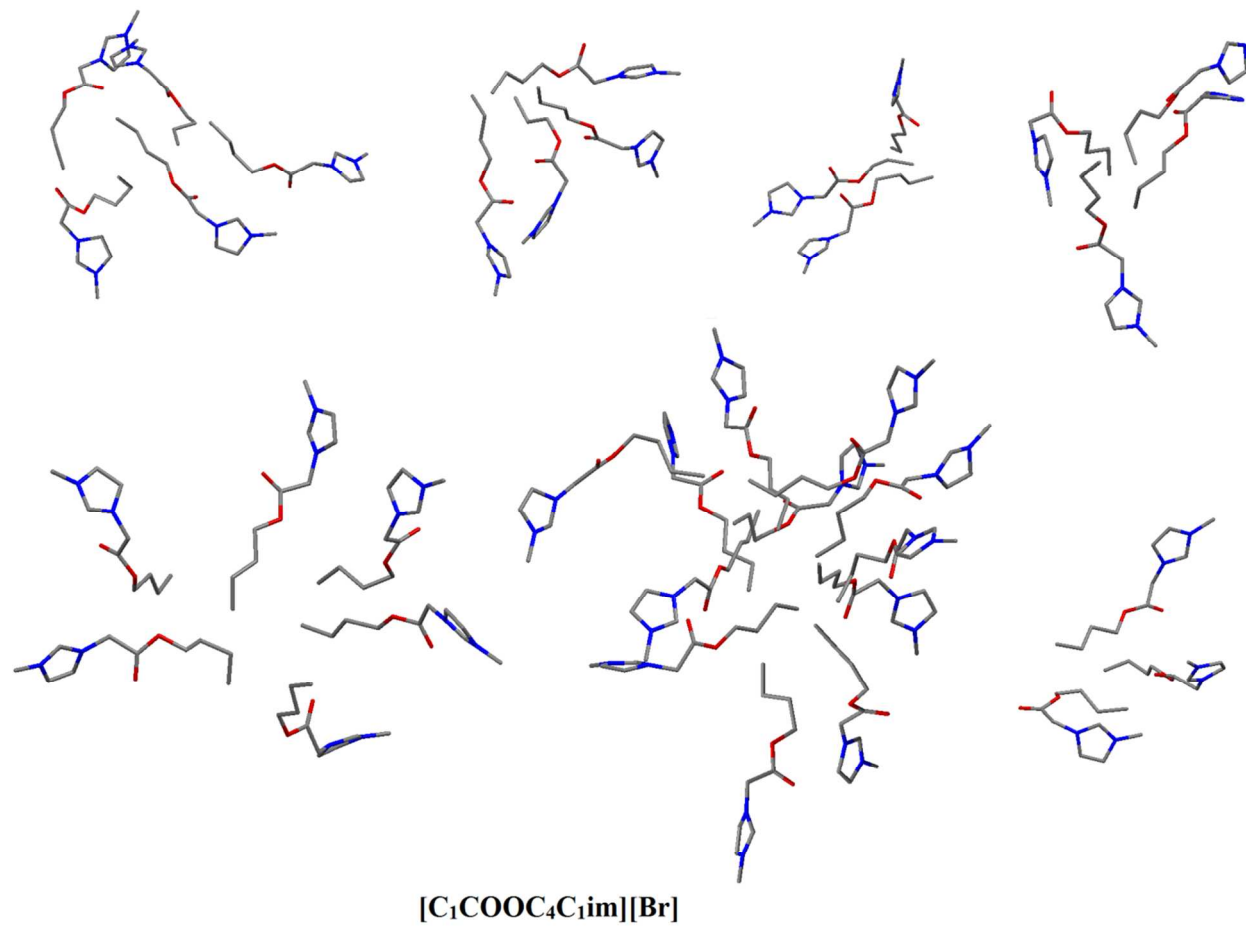
Figure 9.

Figure 10.

Figure 11.

O_8--H_2

O_8--H_5

O_8--H_{11}

O_8--H_{12}

Figure 12.

O₉--H₂

O₉--H₄

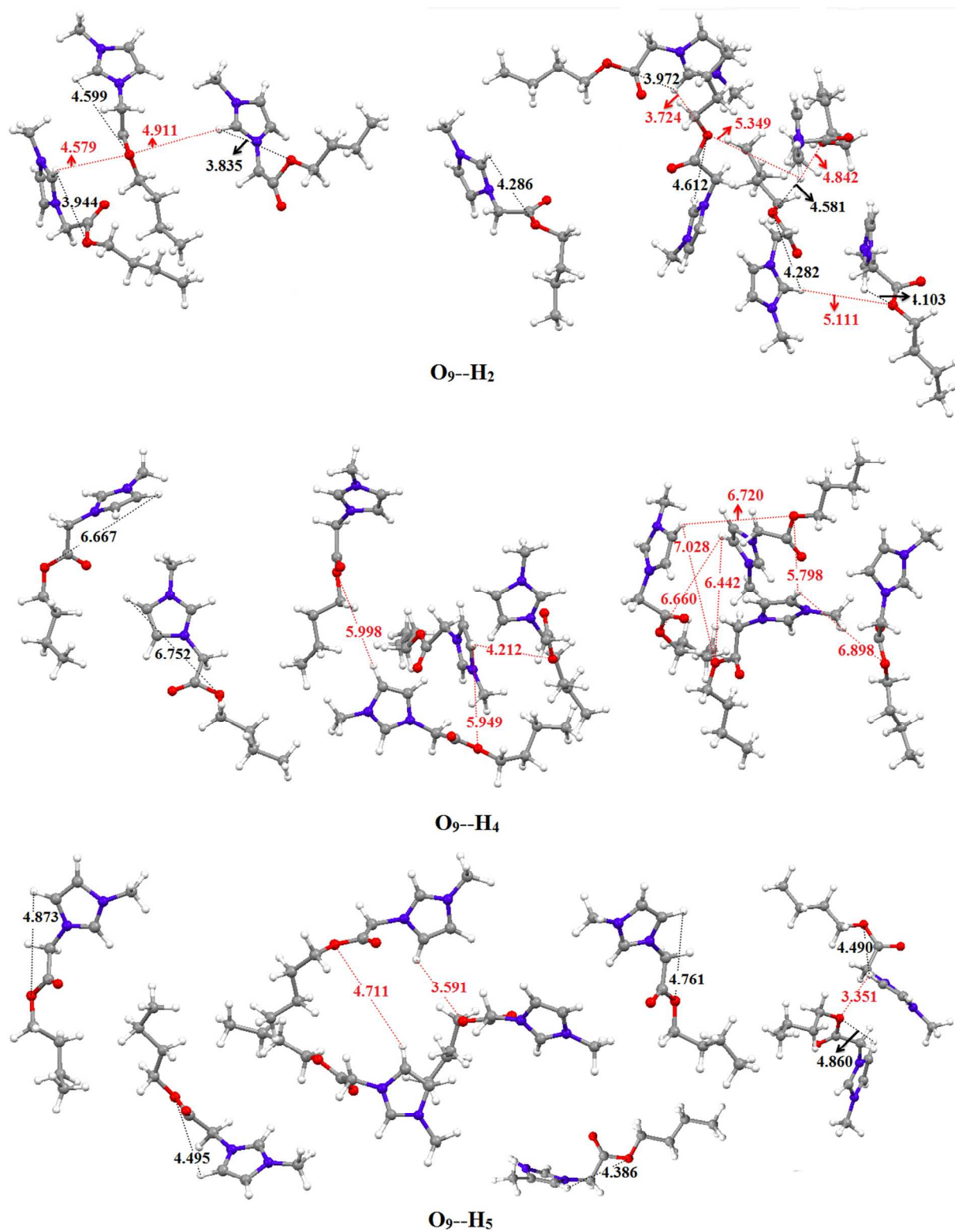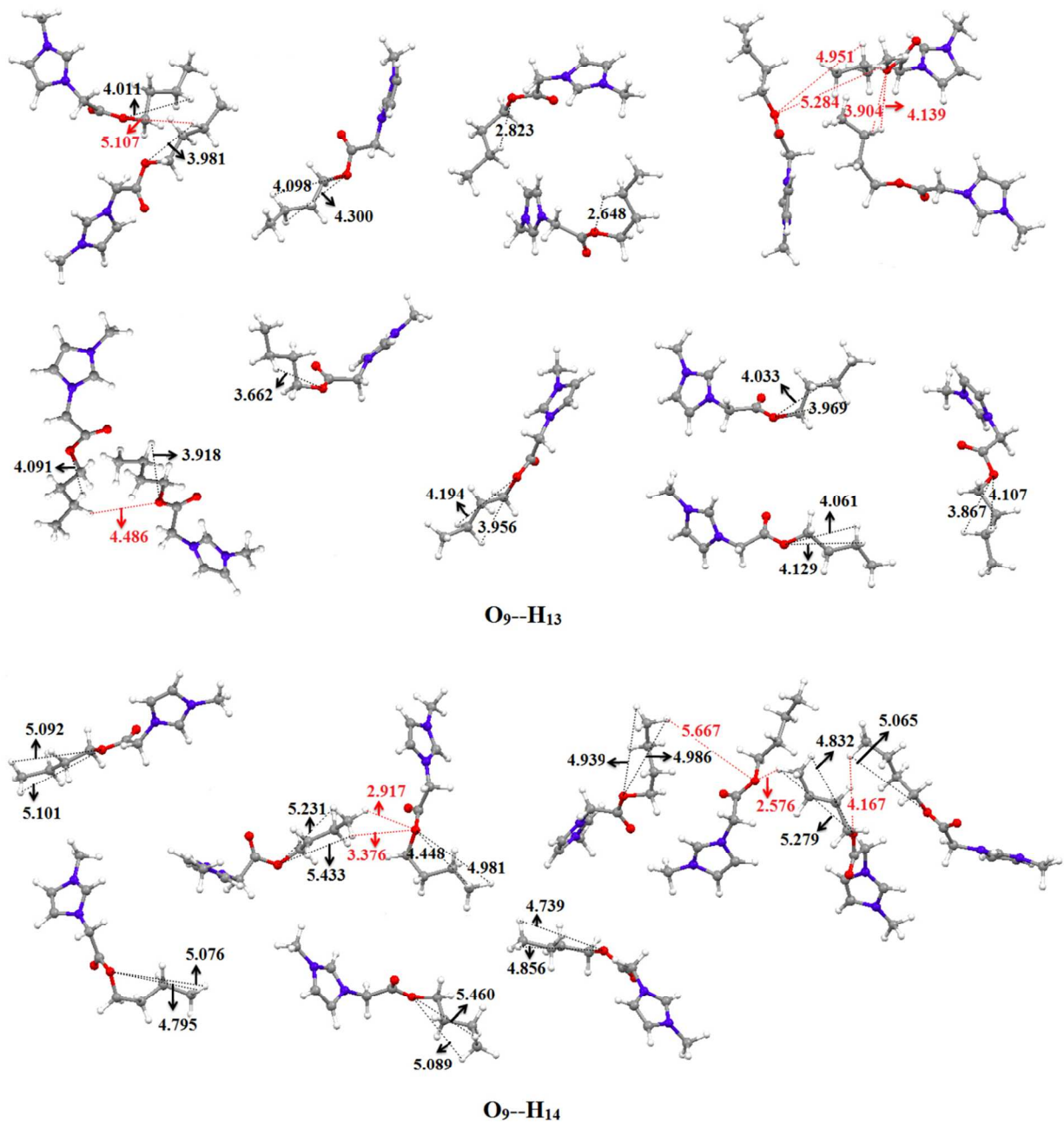O₉--H₅

Figure 13.

$O_9\text{--}H_{13}$

$O_9\text{--}H_{14}$
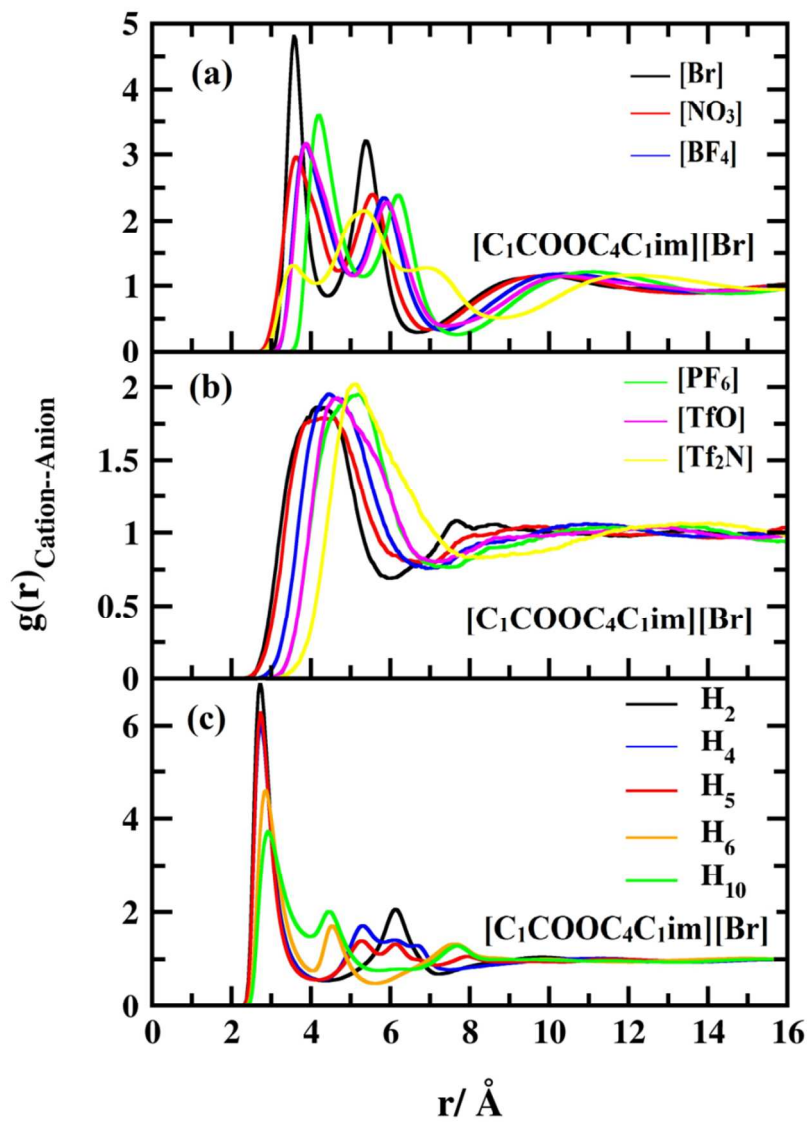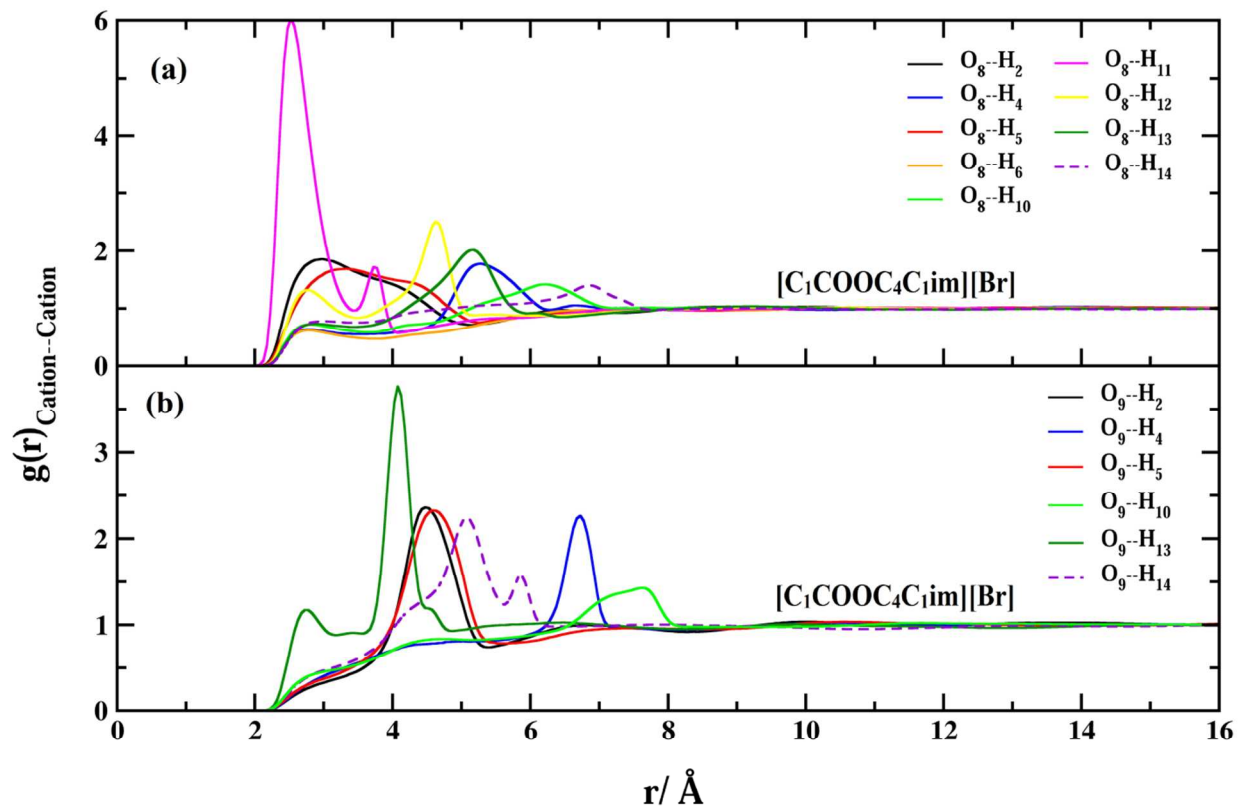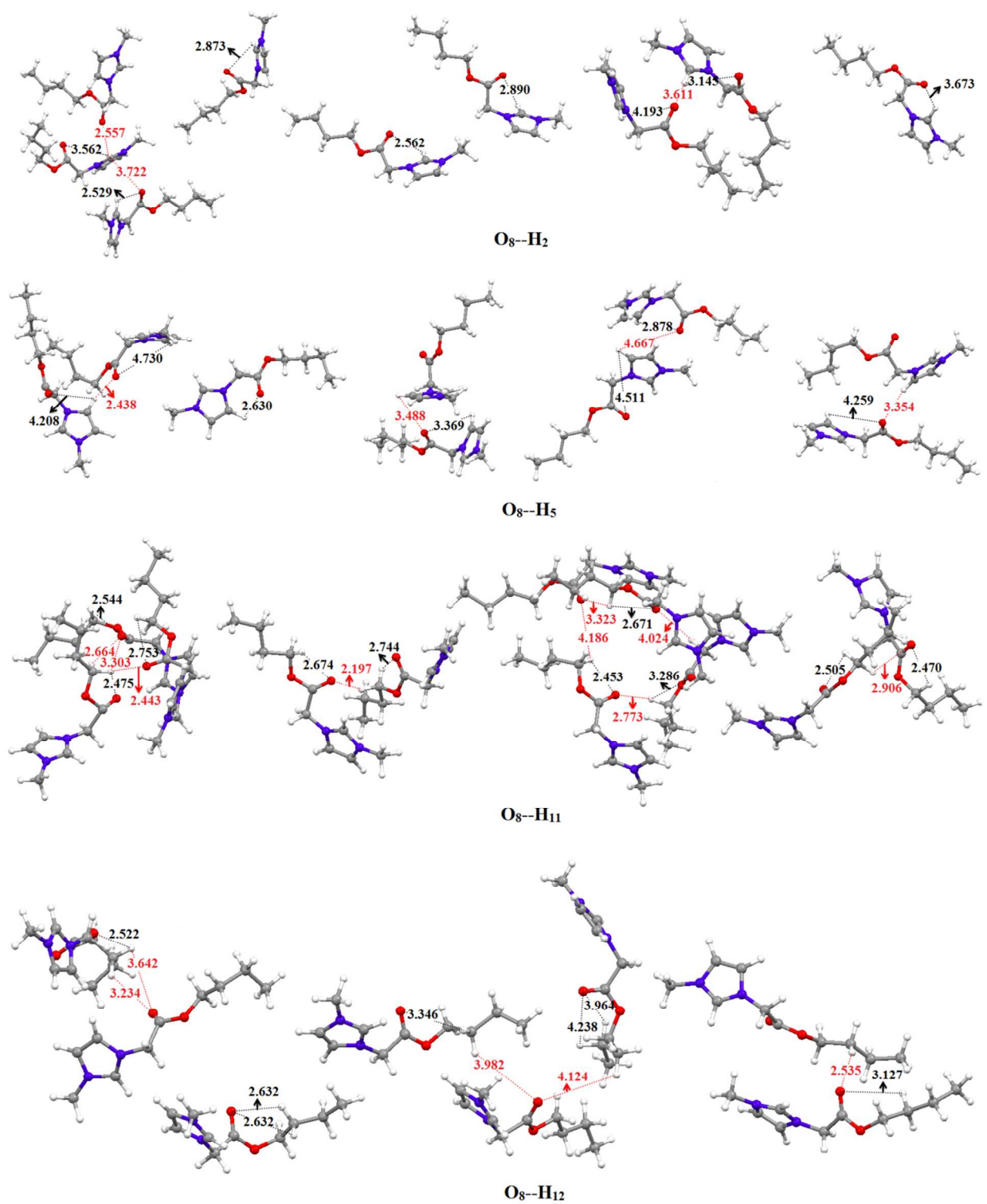
Figure 14.

For Table of Contents Only